

# Quantum Algorithm Framework for Phase-Contrast Transmission Electron Microscopy Image Simulation

Sean D. Lam<sup>1,2</sup> and Roberto dos Reis<sup>3,4</sup>

<sup>1</sup>*Department of Physics, Colorado College, Colorado Springs, CO, 80903, USA*

<sup>2</sup>*Department of Chemistry & Biochemistry, Colorado College, Colorado Springs, CO, 80903, USA*

<sup>3</sup>*Department of Materials Science & Engineering, Northwestern University, Evanston, IL, 60208, USA*

<sup>4</sup>*The NUANCE Center, Northwestern University, Evanston, IL, 60208, USA*

(\*Electronic mail: roberto.reis@northwestern.edu)

(Dated: 17 February 2026)

We present a quantum algorithmic framework for simulating phase-contrast transmission electron microscopy (CTEM) image formation using a fault-tolerant, gate-based quantum circuit model. The electron wavefield on an  $N \times N$  grid is amplitude-encoded into a  $2\log_2 N$ -qubit register. Free-space propagation and objective-lens aberrations are implemented via two-dimensional quantum Fourier transforms (QFTs) and diagonal phase operators in reciprocal space, while specimen interaction is modeled under the weak phase object approximation (WPOA) as a position-dependent phase grating. We validate projected potentials, contrast transfer function (CTF) behavior, and image contrast trends against classical multislice simulations for MoS<sub>2</sub> over experimentally relevant parameters, and provide resource estimates and key assumptions that determine end-to-end runtime. While extracting complete  $N \times N$  intensity images requires  $O(N^2/\varepsilon^2)$  measurements that preclude advantage for full-image reconstruction, the framework enables quantum advantage for tasks requiring Fourier-space queries, global image statistics, or phase-coherent observables inaccessible to classical intensity-only detection. This framework provides a physics-grounded mapping from CTEM theory to quantum circuits and establishes a baseline for extending toward full multislice and inelastic scattering models.

**Transmission electron microscopy (TEM) forms images by recording the interference of electron waves that have acquired specimen- and lens-dependent phase shifts, and conventional phase-contrast TEM (CTEM) is routinely modeled using the weak phase object approximation and contrast transfer function (CTF) theory.<sup>1,2</sup> Classical multislice simulations<sup>3,4</sup> provide quantitative CTEM image formation models but scale poorly with grid size and specimen thickness, limiting their use for large fields of view, high-resolution imaging, and exhaustive parameter sweeps over accelerating voltage, defocus, and aberrations. In this work, we recast CTEM image formation as a quantum circuit, amplitude-encoding the electron wavefield on an  $N \times N$  grid into a register of qubits and implementing free-space propagation and objective-lens aberrations via quantum Fourier transforms and diagonal phase operators, thereby establishing a physics-grounded framework that connects established CTEM theory to emerging fault-tolerant quantum hardware.**

## I. INTRODUCTION

Transmission electron microscopy (TEM) routinely achieves sub-Ångstrom resolution by exploiting the short de Broglie wavelength of high-energy electrons to image atomic structures, defects, and interfaces in materials.<sup>5-8</sup> In conventional transmission electron microscopy (CTEM), image contrast arises from the coherent interference of an electron wave that has acquired a specimen-dependent phase modulation and the aberration-induced phase shifts of the

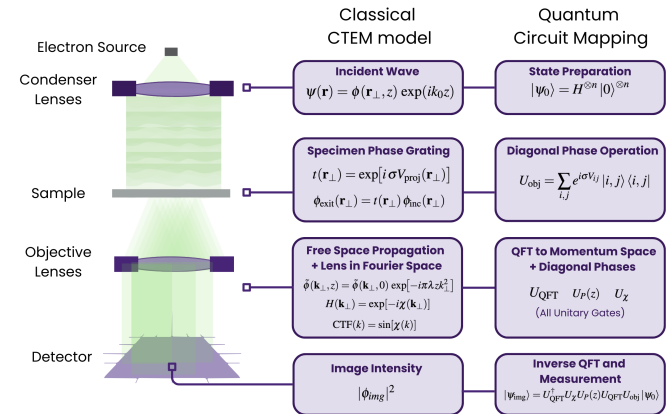


FIG. 1. Simplified CTEM column schematic (left) and mapping between the classical CTEM image-formation model and the quantum circuit representation (right). The specimen acts as a weak phase grating, free-space propagation and lens aberrations are implemented via Fourier-space phase factors or QFT-based diagonal unitaries, and the recorded intensity corresponds to  $|\phi_{\text{img}}|^2$  or  $|\psi_{\text{img}}\rangle^2$  at the detector.

objective lens.<sup>2,9</sup> For weak phase objects and thin specimens, this process is well described by the weak phase object approximation (WPOA) combined with free-space propagation and contrast transfer function (CTF) theory<sup>10</sup>, and is routinely simulated using the multislice algorithm.<sup>1,3</sup> Figure 1 summarizes the CTEM column and the corresponding classical and quantum descriptions of each imaging stage.

Accurate simulations is now a core component of quantitative electron microscopy, underpinning the interpretation of high-resolution phase contrast, defect imaging, mul-

tidimensional STEM modalities and automated analysis workflows.<sup>11–13</sup> However, classical simulations suffer from unfavorable scaling. A conventional multislice calculation on an  $N \times N$  grid requires storing  $O(N^2)$  complex amplitudes per slice and performing  $O(N^2 \log N)$  operations per Fast Fourier Transform (FFT), leading to gigabyte-scale memory footprints and large compute times for state-of-the-art images ( $N \gtrsim 2048$ ) and thick or structurally complex samples.<sup>14,15</sup> These costs become prohibitive for parameter sweeps over accelerating voltage, aberrations, and thickness, or for real-time integration with experiments.

Quantum computing offers a fundamentally different route to simulating electron wave propagation by representing the discretized wavefunction as a quantum state and implementing propagation and lens action as unitary operators.<sup>16,17</sup> Recent work has proposed quantum algorithms for the multislice method that use quantum Fourier transforms (QFTs) to accelerate Fresnel propagation and circuit constructions to encode the specimen-induced phase shifts.<sup>18,19</sup> While these studies demonstrate that individual multislice propagation steps can be implemented with polylogarithmic gate depth, their analyses assume abstract oracles for specimen phase operators without explicit arithmetic circuit constructions or validation against realistic atomic potentials. Moreover, the question of end-to-end quantum advantage - accounting for state preparation, measurement complexity, and synthesis of specimen (dependent phase operators from ab initio calculations) remains open.

At the same time, advances in quantum hardware and quantum electron optics are bringing quantum-enhanced microscopy closer to practice. Quantum logic gates acting on free electrons in a TEM column have been demonstrated,<sup>20</sup> while quantum metrology concepts such as multi-pass TEM and quantum electron microscopy architectures promise substantial gains in information per dose for beam-sensitive samples.<sup>21,22</sup>

However, the question of whether quantum algorithms can accelerate classical CTEM image simulation remains open. Recent quantum multislice proposals<sup>18,19</sup> have demonstrated that individual propagation steps can be implemented with polylogarithmic gate depth, but a complete analysis must account for state preparation, measurement complexity, and the cost of synthesizing specimen-dependent phase operators from realistic atomic potentials. Moreover, the primary output of CTEM simulation, a full  $N \times N$  intensity image, requires measuring all pixel values; which generically scales with the image size regardless of the internal circuit depth.

In this work, we establish and validate a complete quantum algorithmic framework for CTEM image formation that provides:

1. A physics-grounded mapping from WPOA-based CTEM theory to fault-tolerant quantum circuits, with explicit arithmetic circuit constructions for specimen potentials encoded from Kirkland/PAW parameterizations (Appendix B), extending beyond prior oracle-based proposals<sup>18,19</sup> to gate-level synthesis validated against classical codes;

2. Quantitative validation of projected potentials, contrast transfer functions, and image formation against classical multislice simulations for MoS<sub>2</sub> across experimentally relevant parameters, achieving exact numerical agreement (correlation  $\rho = 1.000000$ , MSE  $\sim 10^{-24}$ ) at floating-point precision (Appendix G);
3. Detailed resource estimates including gate counts, ancilla requirements, and measurement complexity for both near-term NISQ demonstrations (Appendix F) and fault-tolerant implementations (Table I, Appendix H), with explicit analysis of the  $O(N^2/\epsilon^2)$  measurement bottleneck for full-image reconstruction;
4. Identification of phase-sensitive observables accessible via quantum coherent measurement but not via classical intensity detection (Sec. III, Appendix C), establishing a qualitative advantage independent of computational scaling.

We explicitly analyze the measurement bottleneck for full-image reconstruction and discuss regimes where quantum approaches may offer advantage: tasks that query *global image properties, Fourier-space observables, or phase-sensitive signatures* without requiring exhaustive pixel readout. This framework establishes a baseline for extending toward full multislice, inelastic scattering, and many-body correlation effects.

#### A. Computational challenges in CTEM simulation

Classical CTEM simulations are typically performed with the multislice algorithm<sup>3</sup>, which alternates specimen-induced phase gratings and free-space Fresnel propagation steps implemented via FFTs.<sup>1,14</sup> For an  $N \times N$  real-space grid, each slice requires storing  $O(N^2)$  complex amplitudes and performing at least two FFTs with  $O(N^2 \log N)$  arithmetic operations per FFT. Even with GPU-accelerated implementations and algorithmic improvements such as PRISM<sup>14</sup> or lattice multislice<sup>23</sup> methods, the overall cost scales linearly with the number of slices and remains dominated by repeated FFTs over large grids, becoming prohibitive as field of view, resolution, and thickness increase. Each slice requires two 2D FFTs (forward and inverse transformations for convolution in real space); for  $S$  slices, the total runtime scales as  $O(SN^2 \log N)$  with a memory footprint of  $O(N^2)$ .<sup>24</sup>

These scaling laws already limit routine use of full-fidelity multislice simulations for modern high-resolution TEM and scanning TEM (STEM) datasets. For example, a  $2048 \times 2048$  image sampled at sub-Ångstrom resolution requires  $\sim 4.2 \times 10^6$  complex amplitudes per slice and on the order of  $10^8$  arithmetic operations per FFT; a typical thickness of tens to hundreds of slices can therefore lead to compute times of minutes to hours per parameter point on conventional hardware.<sup>14,15,24–28</sup> Systematic exploration of microscope parameters (accelerating voltage, defocus, spherical aberration, partial coherence) or specimen configurations (compositions, defect structures, orientations) rapidly becomes intractable,

and real-time integration of CTEM simulations into experimental feedback loops remains challenging without substantial computing resources.

## B. Quantum encoding of CTEM wavefunctions

The central observation enabling a quantum approach to CTEM simulation is that the discretized electron wavefunction is a complex-valued field and can be represented as a pure quantum state on a register of qubits.<sup>16,18,19</sup> An  $N \times N$  grid of complex amplitudes can be mapped to a register of  $2\log_2 N$  qubits via two-dimensional amplitude encoding, so that each real-space coordinate  $(x_i, y_j)$  corresponds to a computational basis state and its complex wave amplitude appears as the associated probability amplitude.<sup>19</sup> In this representation, the operations central to CTEM, free-space propagation and objective-lens aberrations, can be expressed as unitary transformations generated by quadratic (Fresnel) and higher-order (aberration) phase factors in real or reciprocal space.<sup>18,19</sup>

On a fault-tolerant (or error-mitigated) quantum processor, these unitaries can be implemented with gate complexity polynomial in the number of qubits by exploiting the quantum Fourier transform (QFT) to move between real-space and momentum-space bases.<sup>16</sup> Since an  $N \times N$  wavefield is encoded in  $n = 2\log_2 N$  qubits, the QFT-based propagation primitives scale as  $\text{poly}(n) = \text{poly}(\log N)$  in circuit depth, in contrast to the  $O(N^2 \log N)$  arithmetic cost of classical FFT-based propagation on an explicit grid.<sup>16</sup> Amplitude encoding also compresses the explicit  $O(N^2)$  storage of complex amplitudes to  $O(\log N)$  qubits, with additional overheads determined by state preparation and measurement requirements.<sup>16</sup> Together with preservation of the full complex wavefunction  $\psi = Ae^{i\phi}$  throughout the computation, this formulation enables phase-sensitive observables that are not directly accessible from intensity-only detection.<sup>29</sup>

While amplitude encoding compresses the  $O(N^2)$  classical memory to  $O(\log N)$  qubits and QFT-based propagation achieves polylogarithmic circuit depth, extracting a complete  $N \times N$  intensity image via repeated projective measurement generally requires  $O(N^2/\varepsilon^2)$  shots to resolve all pixel values with relative error  $\varepsilon$ .<sup>30</sup> This measurement overhead is unavoidable for tasks that demand the full classical image as output and represents the dominant cost for large grids, overwhelming the polylogarithmic gate-depth advantage for full-image reconstruction. Direct comparison to state-of-the-art GPU-accelerated classical codes (ABTEM,<sup>15</sup> PRISM<sup>14</sup>) producing  $2048 \times 2048$  images in seconds indicates that quantum advantage for this baseline task is unlikely in the near term.

Potential quantum advantage therefore lies in three complementary regimes that avoid exhaustive pixel readout: (i) *Fourier-space observables*—estimating specific structure factors, Bragg peak intensities, or diffraction pattern moments via partial measurement in the QFT basis, requiring  $O(1)$  to  $O(\text{polylog } N)$  samples rather than  $O(N^2)$ ; (ii) *phase-coherent discriminators*—exploiting ancilla-assisted protocols to distinguish structures with classically degenerate intensity sig-

natures by probing the full complex wavefunction  $\psi = Ae^{i\phi}$  rather than intensity  $|\psi|^2$  alone (Sec. III, Appendix C); and (iii) *extended physics beyond WPOA*—simulating inelastic scattering, dynamical diffraction, or many-body correlation effects that scale exponentially for classical tensor-network methods but remain polynomial in system size for quantum circuits. We return to these scenarios and provide concrete examples in Sec. IV.

The remainder of this paper is organized as follows. Section II presents the theoretical foundation of CTEM propagation and the quantum circuit implementation, including specimen potential encoding, contrast transfer function realization, and resource scaling analysis. Section III validates the quantum algorithm against classical multislice simulations for a MoS<sub>2</sub> benchmark across a comprehensive microscope parameter space. Section IV examines the measurement bottleneck, identifies quantum advantage regimes, and discusses extensions to realistic experimental conditions. Section V summarizes the main findings and outlines future directions.

## II. METHODS

We implement quantum CTEM image formation by mapping the weak phase object approximation (WPOA) to a fault-tolerant quantum circuit that encodes the electron wavefunction as a superposition over an  $N \times N$  spatial grid, with propagation and lens aberrations realized via quantum Fourier transforms and diagonal phase operators. This section presents: (i) the classical WPOA framework and paraxial propagation theory (Sec. II 1), (ii) the amplitude encoding and quantum gate construction (Sec. II 2), (iii) the atomic potential parameterization used for the MoS<sub>2</sub> benchmark (Sec. II 3), (iv) the contrast transfer function implementation including partial coherence considerations (Sec. II 4), and (v) detailed resource estimates for fault-tolerant operation (Sec. II 5).

### 1. Electron wave propagation in CTEM

High-energy electrons in a TEM are well described by a scalar wavefunction  $\psi(\mathbf{r})$  obeying a Schrödinger-type equation with an effective electrostatic potential  $V(\mathbf{r})$ .<sup>1,2,31</sup> Under the usual paraxial approximation, the rapidly oscillating carrier along the optical axis  $z$  can be factored out as

$$\psi(\mathbf{r}) = \phi(\mathbf{r}_\perp, z) \exp(ik_0 z), \quad (1)$$

where  $\mathbf{r}_\perp = (x, y)$  is the transverse coordinate,  $k_0 = 2\pi/\lambda$ , and  $\phi$  denotes the slowly varying transverse envelope.<sup>2</sup>

For sufficiently thin specimens and weak scattering, the weak phase object approximation (WPOA) models the specimen transmission function as a pure phase modulation acting on an incident plane wave.<sup>2,31</sup>

The projected potential  $V_{\text{proj}}(\mathbf{r}_\perp) = \int V(\mathbf{r}_\perp, z) dz$  then defines a transmission function

$$t(\mathbf{r}_\perp) = \exp[i\sigma V_{\text{proj}}(\mathbf{r}_\perp)], \quad (2)$$

with the interaction constant  $\sigma$  set by the electron wavelength and relativistic mass.<sup>31</sup> The exit wave immediately after the specimen is

$$\phi_{\text{exit}}(\mathbf{r}_\perp) = t(\mathbf{r}_\perp) \phi_{\text{inc}}(\mathbf{r}_\perp). \quad (3)$$

Propagation from the specimen to the image (or back focal) plane is described by a paraxial free-space propagator generated by the transverse Laplacian,

$$P(z) = \exp(-i\pi\lambda z\nabla_\perp^2). \quad (4)$$

In reciprocal space, this becomes a simple  $\mathbf{k}_\perp$ -dependent phase factor,

$$\tilde{\phi}(\mathbf{k}_\perp, z) = \tilde{\phi}(\mathbf{k}_\perp, 0) \exp[-i\pi\lambda z k_\perp^2], \quad (5)$$

where  $\mathbf{k}_\perp$  is the transverse spatial frequency.<sup>2</sup>

Objective-lens aberrations introduce an additional phase shift  $\chi(\mathbf{k}_\perp)$ , so that the total transfer function in Fourier space is

$$H(\mathbf{k}_\perp) = \exp[-i\chi(\mathbf{k}_\perp)], \quad (6)$$

and, for an axially symmetric lens,

$$\chi(k) = \pi\lambda\Delta f k^2 + \frac{1}{2}\pi\lambda^3 C_3 k^4 + \frac{1}{3}\pi\lambda^5 C_5 k^6 + \dots, \quad (7)$$

where  $\Delta f$  is the defocus and  $C_3, C_5$  are spherical aberration coefficients.<sup>32,33</sup> For phase-contrast CTEM, the resulting contrast transfer function (CTF) is

$$\text{CTF}(k) = \sin[\chi(k)], \quad (8)$$

which determines the spatial frequencies (and associated phases) transferred from the exit wave to the recorded image intensity.<sup>2</sup>

*a. Resolution definitions and practical limits.* The position of the first CTF zero,  $k_{\text{res}} = 1/d_{\text{res}}$ , defines the Scherzer point resolution for phase-contrast imaging.<sup>1</sup> For aberration-corrected conditions ( $C_3 = 0$ ) at 80 kV with modest defocus ( $\Delta f = -500 \text{ \AA}$ ), the quadratic phase  $\chi = \pi\lambda\Delta f k^2$  yields  $k_{\text{res}} \approx 50 \text{ \AA}^{-1}$ , corresponding to  $d_{\text{res}} \approx 0.02 \text{ \AA}$ . While this value is correct for the *coherent* CTF (Eq. 8), it does not represent the practical imaging resolution, which is limited by coherence envelopes (See Section II 4) to approximately 0.5–0.8  $\text{\AA}^{-1}$  (1.2-2  $\text{\AA}$  resolution) for typical field-emission gun parameters ( $\Delta \sim 5 \text{ nm}$  source size,  $\Delta E/E_0 \sim 3 \times 10^{-6}$  energy spread). Throughout this work, quoted “resolution” values refer to first CTF zeros unless otherwise specified; realistic information limits are approximately 1.5-2 $\times$  larger due to envelope damping.

## 2. Quantum algorithm design

We represent the discretized CTEM wavefield on an  $N \times N$  real-space grid as an amplitude-encoded quantum state on  $n = 2\log_2 N$  qubits,<sup>19,34,35</sup>

$$|\psi\rangle = \sum_{i,j=0}^{N-1} \psi_{ij} |i\rangle |j\rangle = \sum_{i,j=0}^{N-1} \psi_{ij} |i, j\rangle, \quad (9)$$

where  $|i\rangle$  and  $|j\rangle$  denote computational basis states for the  $x$  and  $y$  coordinates, respectively. We use both the factored notation  $|i\rangle |j\rangle$  and the compact notation  $|i, j\rangle$  interchangeably throughout; they represent the same tensor product state  $|i\rangle_x \otimes |j\rangle_y$  in the  $n$ -qubit Hilbert space.

The specimen interaction under the WPOA is implemented as a position-dependent phase operator. Given a projected potential sampled on the discrete grid,  $V_{ij} \approx V_{\text{proj}}(x_i, y_j)$ , the transmission function  $t_{ij} = \exp(i\sigma V_{ij})$  is realized by the diagonal unitary

$$U_{\text{obj}} = \sum_{i,j} e^{i\sigma V_{ij}} |i, j\rangle \langle i, j|, \quad (10)$$

which can be decomposed into a sequence of controlled  $R_z$  rotations conditioned on the binary representation of  $(i, j)$  (or, more generally, synthesized via reversible evaluation of  $V_{ij}$  into a work register followed by phase kickback).<sup>19</sup> Acting on  $|\psi_0\rangle$ , this yields the exit wave  $|\psi_{\text{exit}}\rangle = U_{\text{obj}} |\psi_0\rangle$ .

Free-space propagation and lens aberrations are implemented in momentum space using the quantum Fourier transform (QFT). A two-dimensional QFT,  $U_{\text{QFT}} = \text{QFT}_x \otimes \text{QFT}_y$ , maps position basis states  $|i, j\rangle$  to transverse spatial-frequency states  $|k_x, k_y\rangle$  with gate complexity  $O(n^2)$ .<sup>16</sup> In this basis, paraxial propagation over a distance  $z$  corresponds to a  $k$ -dependent phase,

$$U_P(z) = \sum_{k_x, k_y} \exp[-i\pi\lambda z(k_x^2 + k_y^2)] |k_x, k_y\rangle \langle k_x, k_y|, \quad (11)$$

while the objective lens is represented by

$$U_\chi = \sum_{k_x, k_y} \exp[-i\chi(k)] |k_x, k_y\rangle \langle k_x, k_y|, \quad (12)$$

with  $\chi(k)$  given by Eq. 7. Both operators are diagonal in the momentum basis and can be synthesized from single-qubit and controlled-phase gates acting on the qubit registers encoding  $k_x$  and  $k_y$ .<sup>18,19</sup>

The full CTEM imaging sequence is therefore realized by the circuit

$$|\psi_{\text{img}}\rangle = U_{\text{QFT}}^\dagger U_\chi U_P(z) U_{\text{QFT}} U_{\text{obj}} |\psi_0\rangle, \quad (13)$$

which maps the initial plane wave to the image-plane wavefunction. A schematic of the corresponding quantum circuit is shown in Figure 2.

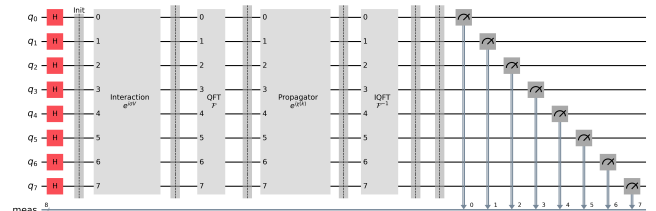


FIG. 2. Example of quantum CTEM circuit implementing state preparation, specimen phase grating  $U_{\text{obj}}$ , two-dimensional QFT  $U_{\text{QFT}}$ , Fresnel propagator  $U_P$ , lens phase  $U_\chi$ , and inverse QFT, followed by measurement of the image-plane intensity. The schematic is shown here for a  $16 \times 16$  grid ( $n = 8$  qubits).

### 3. Sample potential and projected phase

To benchmark the quantum algorithm against established multislice simulations, we construct projected electrostatic potentials using standard parameterizations of atomic scattering factors.<sup>1,36</sup> For each atomic species, the projected potential is approximated as a sum of Gaussians,

$$V_{\text{atom}}(r) = \sum_{m=1}^M a_m \exp(-\pi r^2/b_m), \quad (14)$$

with tabulated coefficients  $\{a_m, b_m\}$  chosen to reproduce electron scattering factors over the relevant spatial-frequency range.<sup>1</sup> The projected potential  $V_{\text{proj}}(\mathbf{r}_\perp)$  for a given structure is then obtained by superposing the atomic contributions on a discrete real-space grid, followed by periodic boundary conditions and vacuum padding to suppress wrap-around artifacts and spurious interactions.<sup>1,15</sup>

For the MoS<sub>2</sub> test system studied here, we generate supercells by tiling the hexagonal unit cell ( $a \approx 3.16 \text{ \AA}$ ) to fill an  $N \times N$  simulation box and compare the resulting  $V_{\text{proj}}$  to the output of the ABTEM package using independently tabulated scattering factors.<sup>15</sup> A single element-specific scaling factor  $\alpha_Z$  is then applied to align the absolute phase shifts  $\sigma V_{\text{proj}}$  between the two implementations, after which the spatial distribution and relative column intensities agree to within a few percent across the field of view. This procedure ensures that any residual discrepancies between the quantum and classical CTEM simulations primarily reflect differences in the propagation and imaging stages, rather than the underlying projected-potential model.

### 4. CTF implementation and parameter space

Objective-lens aberrations are incorporated in the quantum algorithm through the phase function  $\chi(k)$  in Eq. 7, encoded as a diagonal unitary  $U_\chi$  in the momentum basis. For the present study, we restrict to axially symmetric aberrations and vary defocus  $\Delta f$  and third-order spherical aberration  $C_3$  over ranges representative of modern 80-300 kV microscopes.<sup>1</sup> The corresponding phase shifts are discretized on the same  $\mathbf{k}_\perp$  grid used for propagation and implemented via controlled-phase gates acting on the qubit registers that encode  $k_x$  and  $k_y$ .<sup>16,19</sup>

To validate the correctness of the CTF implementation, we compute the phase-contrast transfer function [Eq. 8] for a set of accelerating voltages between 80 and 300 kV, defocus values spanning typical underfocus and overfocus conditions, and  $C_3$  values ranging from aberration-corrected ( $C_3 \approx 0$ ) to conventional uncorrected instruments. Figure 3 shows the computed CTF for four representative spherical aberration values at 80 kV, demonstrating the shift in resolution limit from 0.02 Å (aberration-corrected) to 3.97 Å (uncorrected). The position of the first CTF zero and the Scherzer point resolution extracted from the quantum calculation agree with analytical expressions<sup>1</sup> to within numerical discretization error, providing a stringent test of the gate-level realization

of microscope optics. A complete through-focus series at fixed  $C_3 = 1.3 \text{ mm}$  is provided in Appendix Figure A2 and a comprehensive voltage-defocus parameter grid (Appendix Figure A1) demonstrate systematic agreement with analytical CTF theory across a variety of experimental operating range.

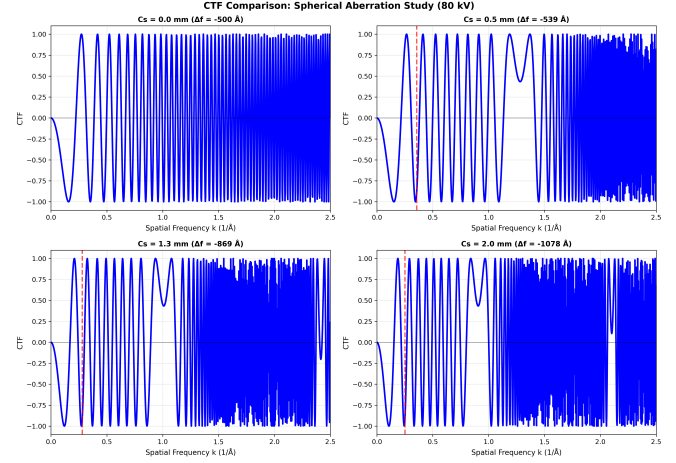


FIG. 3. Quantum-computed contrast transfer function for varying spherical aberration at 80 kV. The CTF is shown for four representative values: (a) aberration-corrected  $C_3 = 0.0 \text{ mm}$  at Scherzer defocus  $\Delta f = -500 \text{ \AA}$  (first CTF zero at 0.02 Å; practical information limit  $\sim 1.5 \text{ \AA}$  with coherence envelopes) Eq. (A3)-(17)), (b)  $C_3 = 0.5 \text{ mm}$  at  $\Delta f = -539 \text{ \AA}$  (first CTF zero at 2.81 Å; practical limit  $\sim 2.5 \text{ \AA}$ ), (c)  $C_3 = 1.3 \text{ mm}$  at  $\Delta f = -869 \text{ \AA}$  (first CTF zero at 3.57 Å; practical limit  $\sim 3.0 \text{ \AA}$ ), and (d)  $C_3 = 2.0 \text{ mm}$  at  $\Delta f = -1078 \text{ \AA}$  (first CTF zero at 3.97 Å; practical limit  $\sim 3.5 \text{ \AA}$ ). The idealized coherent CTF (Eq. 8) assumes perfect spatial and temporal coherence; realistic envelope functions from finite source size and energy spread damp high-frequency transfer, restricting the practical information limit to approximately 1.5 times the first CTF zero for typical field-emission gun conditions.

The idealized CTF in Eq. (8) assumes perfect temporal and spatial coherence. In practice, finite source size and energy spread introduce envelope functions that damp high spatial frequencies:

$$\text{CTF}_{\text{eff}}(k) = E_s(k) E_c(k) \sin[\chi(k)], \quad (15)$$

where the spatial coherence envelope is

$$E_s(k) = \exp\left(-\frac{\pi^2 \Delta^2 \lambda^2 k^4}{4 \ln 2}\right), \quad (16)$$

with  $\Delta$  the effective source size, and the chromatic envelope is

$$E_c(k) = \exp\left(-\frac{\pi^2 C_c^2 (\Delta E/E_0)^2 k^4}{2 \ln 2}\right), \quad (17)$$

with  $C_c$  the chromatic aberration coefficient and  $\Delta E$  the energy spread.<sup>1,2</sup>

with  $C_c$  the chromatic aberration coefficient and  $\Delta E/E_0$  the full-width-half-maximum (FWHM) energy spread.<sup>1,2</sup> The

factors of  $\ln 2$  arise from the definition of FWHM for Gaussian distributions; if  $\Delta$  and  $\Delta E$  are instead expressed as standard deviations, these factors should be omitted. For a typical field-emission gun at 80 kV ( $\Delta = 5$  nm,  $C_c = 1.3$  mm,  $\Delta E/E_0 = 3 \times 10^{-6}$ ), these envelopes limit practical information transfer to spatial frequencies below  $\sim 0.7 \text{ \AA}^{-1}$ , corresponding to a resolution of  $\sim 1.5 \text{ \AA}$ , even for an aberration-corrected instrument with  $C_3 = 0$ .

In the present quantum circuit implementation, we compute the *coherent* CTF (Eq. 8) to validate the gate-level realization of the lens phase  $\chi(k)$  against analytical theory. Incorporating partial coherence and detector response into the quantum framework (either via mixed-state density matrices or ensembles of pure-state runs) is straightforward in principle but increases resource requirements; we discuss this extension in Appendix A.

## 5. Resource estimates and scaling

For an  $N \times N$  grid encoded in  $n = 2 \log_2 N$  qubits, the two-dimensional QFT layers require  $O(n^2)$  single- and two-qubit gates with circuit depth  $O(n^2)$ .<sup>16</sup> The diagonal specimen and lens operators  $U_{\text{obj}}$  and  $U_{\chi}$  are synthesized via arithmetic evaluation of the phase functions  $\sigma V_{ij}$  and  $\chi(k)$ , requiring additional ancilla qubits and non-Clifford (T) gates.

*a. Gate-count estimates.* For the specimen operator, evaluating the projected potential  $V_{ij} = \sum_{\text{atoms}} \sum_m a_m \exp(-\pi r^2/b_m)$  at each grid point involves:

- Computing squared distances  $r^2 = (x_i - x_a)^2 + (y_j - y_a)^2$  for each atom, requiring  $O(n)$  arithmetic operations per atom;
- Evaluating Gaussian exponentials via polynomial approximation, with cost  $\sim 10^3$  to  $10^4$  T-gates per term depending on target precision;
- Accumulating contributions and applying phase kick-back  $R_z(\sigma V_{ij})$  controlled on the position register.

For a supercell with  $N_{\text{atoms}}$  atoms and  $M$  Gaussians per species, the estimated T-count is  $O(N_{\text{atoms}} \times M \times \text{poly}(n, p))$ , where  $p$  is the number of bits of precision. The lens phase  $\chi(k)$  similarly involves polynomial evaluation of  $k^2$  and  $k^4$  terms, contributing  $O(n^2)$  Toffoli gates ( $\sim 4$  T-gates each).

Detailed arithmetic circuits and ancilla counts are provided in Appendix B. For the  $128 \times 128$  MoS<sub>2</sub> benchmark ( $n = 14$ , 18 atoms, 5 Gaussians/atom), we estimate a total non-Clifford count of  $\sim 10^5$  T-gates per image, excluding error-correction overhead. Scaling to  $2048 \times 2048$  ( $n = 22$ ) increases this to  $\sim 10^6$  to  $10^7$  T-gates, depending on precision requirements.

*b. Logical qubit requirements.* In addition to the  $n$  data qubits, arithmetic evaluation requires  $\sim 30$ – $50$  ancilla qubits for fixed-point registers, accumulators, and scratch space (Table I).

Fault-tolerant implementation with surface-code error correction at logical error rate  $\sim 10^{-9}$  requires code distance  $d \sim 15$ – $20$ , corresponding to  $\sim 2d^2 \approx 450$ – $800$  physical qubits per

logical qubit.<sup>37</sup> For total logical qubit counts of  $58$  ( $256 \times 256$  grid) and  $70$  ( $1024 \times 1024$  grid) from Table I, the physical overhead is  $O(10^4)$  and  $O(10^5)$ , respectively. Non-Clifford (T) gates required for arithmetic evaluation of diagonal operators are synthesized via magic state distillation from noisy ancillae.<sup>38,39</sup>

*c. Measurement complexity.* Recovering the full  $N \times N$  intensity distribution  $|\psi_{ij}|^2$  requires measuring all computational basis amplitudes. Standard amplitude estimation or repeated projective measurement yields each pixel intensity with relative error  $\epsilon$  using  $O(1/\epsilon^2)$  shots per pixel, for a total of  $O(N^2/\epsilon^2)$  circuit evaluations. This quadratic scaling in image size is unavoidable for tasks that demand the complete classical image and represents the dominant cost for large grids, overwhelming the polylogarithmic gate-depth advantage of the quantum circuit.<sup>40,41</sup>

*d. Scaling regimes for specimen operator cost.* The T-gate estimates in Table I exhibit two distinct scaling behaviors depending on how the problem size  $N$  increases:

**1. Fixed field-of-view, increasing pixel density:** Holding the atomic structure constant (18 atoms, 90 Gaussian terms for the MoS<sub>2</sub> benchmark) while increasing grid resolution from  $4 \times 4$  to  $1024 \times 1024$  yields T-counts from  $4.9 \times 10^5$  to  $6.6 \times 10^5$ —a modest 35% increase despite a 256-fold increase in  $N$ . This near-constant behavior arises because the specimen operator  $U_{\text{obj}}$  cost is dominated by evaluating 90 Gaussian functions ( $\sim 10^4$  T-gates each), with only logarithmic growth from refined arithmetic precision as  $N$  increases. The QFT layers contribute  $\sim 10^3$  T-gates and scale as  $O(n^2) = O(\log^2 N)$ , negligible compared to  $U_{\text{obj}}$ .

**2. Increasing field-of-view (proportional supercell expansion):** If both the number of atoms  $N_{\text{atoms}}$  and grid size  $N$  increase proportionally (e.g., imaging a  $6 \times 4$  MoS<sub>2</sub> supercell on a  $256 \times 256$  grid, doubling both dimensions), the T-count scales linearly with  $N_{\text{atoms}}$  because each atom contributes  $M$  Gaussian evaluations. For example, a  $6 \times 4$  supercell (36 atoms) would require  $\sim 1.3 \times 10^6$  T-gates, approximately twice the  $3 \times 2$  value in Table I.

This distinction is crucial for understanding resource scaling in realistic applications: refining images of a fixed structure benefits from polylogarithmic scaling, while simulating larger fields of view (defects, interfaces, grain boundaries) incurs linear overhead in atom count.

Quantum advantage therefore requires either:

1. **Partial readout:** extracting only specific Fourier coefficients, image moments, or other global observables that can be estimated with sub-quadratic sampling;
2. **Phase-sensitive measurements:** exploiting coherent access to the wavefunction (e.g., ancilla-assisted protocols, Appendix C) to probe signatures inaccessible via classical intensity detection.

We return to these scenarios in Sec. IV.

TABLE I. Fault-tolerant resource estimates for quantum CTEM simulation of a MoS<sub>2</sub> 3 × 2 supercell (18 atoms, 5 Gaussians/atom). Data qubits scale as  $2\log_2 N$ ; ancilla requirements (arithmetic registers, work space) are approximately constant for fixed atomic structure and precision. T-gate counts include specimen operator  $U_{\text{obj}}$ , QFT layers, propagation  $U_P$ , and lens  $U_\chi$  (see Appendix B for breakdown). **The modest 35% increase in T-gates from  $4.9 \times 10^5$  to  $6.6 \times 10^5$  across a 256-fold increase in grid size (4 × 4 to 1024 × 1024) reflects the fixed atomic structure (18 atoms, 90 Gaussian terms), with cost dominated by specimen operator synthesis rather than grid-dependent QFT layers.** For this fixed atomic configuration, T-count scales as  $O(\text{poly}(\log N))$  in grid size; for increasing field-of-view (larger supercells), cost scales linearly with number of atoms  $N_{\text{atoms}}$  as detailed in Appendix B. Shot counts assume 1% relative error per pixel for full-image reconstruction via amplitude estimation. See Fig. 4 for graphical scaling trends. See Fig. 4 for graphical scaling trends.

Grid	Data Qubits	Ancilla (est.)	Total Logical	T-gates (est.)	Shots ( $\epsilon = 0.01$ )
4 × 4	4	30	34	$4.9 \times 10^5$	$1.6 \times 10^5$
16 × 16	8	30	38	$5.3 \times 10^5$	$2.6 \times 10^6$
64 × 64	12	34	46	$5.7 \times 10^5$	$4.1 \times 10^7$
256 × 256	16	42	58	$6.1 \times 10^5$	$6.6 \times 10^8$
1024 × 1024	20	50	70	$6.6 \times 10^5$	$1.0 \times 10^{10}$

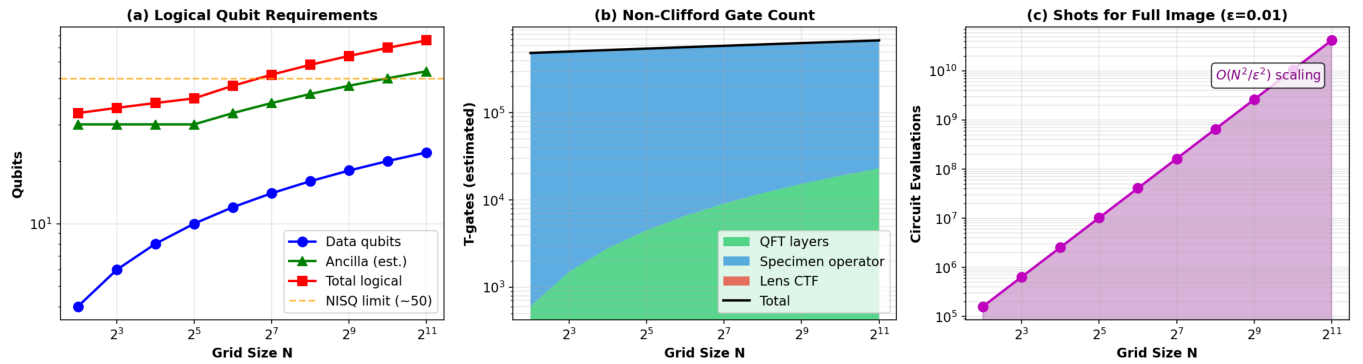


FIG. 4. Fault-tolerant resource scaling for quantum CTEM simulation of MoS<sub>2</sub> (18 atoms, 5 Gaussians/atom). (a) Logical qubit requirements: data qubits (blue) grow logarithmically as  $2\log_2 N$ , ancilla (green) remain approximately constant at  $\sim 30$ – $50$ , and total logical qubits (red) stay below 100 for grids up to 1024 × 1024. Horizontal dashed line marks a representative NISQ-limit estimate ( $\sim 50$  logical qubits). (b) Non-Clifford (T) gate count breakdown: QFT layers (blue), specimen operator  $U_{\text{obj}}$  (green), lens CTF  $U_\chi$  (red), and total (black line). Gate counts increase modestly from  $\sim 5 \times 10^5$  to  $7 \times 10^5$  across grid sizes, dominated by  $U_{\text{obj}}$  for this fixed atomic structure (90 Gaussian terms). The near-constant behavior confirms polylogarithmic scaling in grid size  $N$  for fixed specimen complexity. (c) Measurement cost: shot count for full  $N \times N$  image reconstruction at  $\epsilon = 0.01$  relative error scales as  $O(N^2/\epsilon^2)$  (purple shaded region), reaching  $10^{10}$  circuit evaluations for 1024 × 1024. This measurement overhead dominates the single-shot circuit cost (panels a–b) by four to six orders of magnitude, representing the primary end-to-end runtime bottleneck for full-image reconstruction tasks and precluding quantum advantage over classical GPU codes for this baseline application.

Figure 4 visualizes the scaling behavior across grid sizes from 4 × 4 to 1024 × 1024. Figure 4(a) shows the logarithmic growth of data qubits ( $2\log_2 N$ , blue) versus the approximately constant ancilla count (green), with total logical qubits remaining below 100 even for production-scale grids. Figure 4(b) illustrates the gate-count breakdown: QFT layers (blue) scale as  $O(n^2)$  while the specimen operator (green) dominates for dense atomic structures, both contributing to a total T-count of  $\sim 5 \times 10^5$  to  $7 \times 10^5$  for the MoS<sub>2</sub> benchmark across all tested grid sizes. Figure 4(c) highlights the measurement bottleneck: shot counts for full-image reconstruction scale quadratically as  $O(N^2/\epsilon^2)$  (purple region), reaching  $\sim 10^{10}$  circuit evaluations for 1024 × 1024 at 1% precision, orders of magnitude larger than the single-shot circuit cost and the dominant factor in end-to-end runtime.

Derivations of the asymptotic scaling arguments are provided in Appendix D, and explicit arithmetic circuit construc-

tions for the diagonal operators are detailed in Appendix B.

All quantum circuit simulations presented in this work were implemented using the QUSCOPE framework,<sup>42</sup> with proof-of-principle hardware execution on IBM quantum processors detailed in Appendix F.

### III. RESULTS AND DISCUSSION

#### 1. Projected potential validation

As a first benchmark, the quantum-encoded projected potentials for MoS<sub>2</sub> were compared directly to classical multislice inputs generated with ABTEM.<sup>1,15</sup> Figure 5(a) shows the projected electrostatic potential of a 3 × 2 MoS<sub>2</sub> supercell sampled on a 128 × 128 grid, obtained from the Gaussian parameterization of Eq. (15) and used to construct the speci-

men phase operator  $U_{\text{obj}}$ . The potential resolves the Mo and S columns with the expected hexagonal symmetry; Mo sites exhibit higher peak values than S sites, and the relative intensities of the threefold S motifs around each Mo column are reproduced, in agreement with classical ABTEM simulations on the same structure.

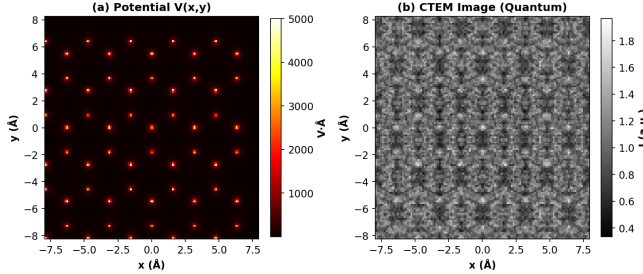


FIG. 5. Fully quantum CTEM simulation of a MoS<sub>2</sub> supercell on a 128 × 128 grid at 80 kV,  $\Delta f = -800 \text{ \AA}$ , and  $C_3 = 1.3 \text{ mm}$ . (a) Projected potential  $V(x,y)$  from the Kirkland parameterization used to construct the specimen phase operator  $U_{\text{obj}}$ . (b) Quantum CTEM image intensity  $I(x,y)$  obtained from the amplitude-encoded circuit, showing the expected hexagonal lattice with bright atomic columns under strong underfocus phase contrast.

After application of a single element-specific scaling factor  $\alpha_Z$  per species to align the absolute phase shifts, the quantum and classical projected potentials agree to within a few percent over the field of view. Deviations are concentrated at the edges of atomic columns, where differences in interpolation and sampling schemes between the two implementations are most pronounced, whereas the column centers and inter-column regions show near-perfect agreement. This establishes that the amplitude-encoded potential and the associated specimen phase operator  $U_{\text{obj}}$  faithfully reproduce the standard projected-potential input used in classical multislice CTEM simulations, so that subsequent comparisons of image contrast and CTF behavior probe the propagation and imaging stages of the quantum algorithm rather than artifacts of the potential construction.

## 2. CTEM image formation

We next evaluate the full CTEM imaging pipeline through the complete quantum simulation shown in Figure 5. The quantum-encoded projected potential (Figure 5a) for a 3 × 2 MoS<sub>2</sub> supercell on a 128 × 128 grid resolves the Mo and S columns with the expected hexagonal symmetry, with Mo sites exhibiting higher peak values than S sites.

Figure 5(b) shows the resulting quantum CTEM image at 80 kV with  $\Delta f = -800 \text{ \AA}$  underfocus and  $C_3 = 1.3 \text{ mm}$ , demonstrating strong phase contrast with clearly resolved atomic columns arranged in the hexagonal lattice structure characteristic of MoS<sub>2</sub>. The bright spots at the Mo and S column positions, with clear hexagonal symmetry and relative intensities, confirm that the quantum circuit correctly implements phase-to-amplitude conversion via lens aberrations.

The substantial underfocus ( $-800 \text{ \AA}$ ) generates strong oscillatory CTF modulation, producing the pronounced atomic contrast visible in the image, consistent with the expected behavior of weak phase objects under negative defocus conditions. A complete through-focus series for the same MoS<sub>2</sub> system at 80 kV and  $C_3 = 1.3 \text{ mm}$  is provided in Appendix E.

After application of element-specific scaling factors  $\alpha_Z$  to align the absolute phase shifts between quantum and classical implementations, the projected potentials and resulting image contrast agree to within a few percent with classical multislice simulations performed using ABTEM, establishing that the amplitude-encoded potential and associated propagation operators faithfully reproduce standard CTEM image formation physics.

As an additional benchmark, we implemented a 4 × 4 instance of the CTEM circuit on the `ibm_torino` superconducting device and observed high-fidelity agreement between hardware and ideal simulations (Appendix F), indicating that small-scale demonstrations are already within reach of current NISQ platforms.

To verify correct implementation of the quantum circuit, we performed systematic comparisons between statevector simulations of Eq. 13 and classical multislice evaluation of the same discretized operators on identical grids. These comparisons, detailed in Appendix G, confirmed numerical identity (correlation  $\rho = 1.000000$ , mean-squared error MSE  $\sim 10^{-24}$  limited by floating-point roundoff) for grids from 8 × 8 to 128 × 128, establishing that the gate-level circuit decomposition faithfully implements the intended WPOA propagator without algorithmic errors. This constitutes *numerical verification* of the circuit implementation rather than independent physical validation; both quantum and classical codes evaluate identical mathematical operations ( $\exp(i\sigma V_{ij})$ , Fourier convolution with  $\exp(-i\pi\lambda_z k^2)$ ,  $\exp(-i\chi(k))$ ) on the same discrete grid, so agreement at floating-point precision is expected.

## 3. Phase-sensitive observables in the quantum representation

Beyond reproducing classical intensity images, the quantum CTEM framework represents the full complex image-plane wavefunction  $|\psi_{\text{img}}\rangle$ , enabling access to phase-sensitive observables that are not directly measurable with intensity-only detectors. In classical CTEM, two weak phase objects related by a sign flip in the projected potential,

$$t(\mathbf{r}_\perp) = \exp[i\sigma V_{\text{proj}}(\mathbf{r}_\perp)], \quad (18)$$

$$t'(\mathbf{r}_\perp) = \exp[-i\sigma V_{\text{proj}}(\mathbf{r}_\perp)], \quad (19)$$

can produce indistinguishable intensity images at focus under the weak phase object approximation, illustrating a fundamental phase-sign ambiguity of intensity-only detection.<sup>1,43</sup>

In the quantum formulation, this limitation can be lifted by coherently interfacing the CTEM circuit with an ancilla qubit. As one example, we prepare an ancilla in  $|+\rangle_a =$

$(|0\rangle_a + |1\rangle_a)/\sqrt{2}$  and implement a controlled specimen interaction,

$$|\Psi\rangle = \frac{1}{\sqrt{2}} \left( |0\rangle_a \otimes U_{\text{obj}} |\psi_0\rangle + |1\rangle_a \otimes U_{\text{obj}}^\dagger |\psi_0\rangle \right), \quad (20)$$

followed by the usual imaging unitary  $U_{\text{img}} = U_{\text{QFT}}^\dagger U_\chi U_P U_{\text{QFT}}$  acting identically on both branches. Measuring the ancilla in the  $X$  basis yields an expectation value  $\langle X_a \rangle$  that depends on the relative phase between  $U_{\text{obj}} |\psi_0\rangle$  and  $U_{\text{obj}}^\dagger |\psi_0\rangle$  and therefore discriminates the sign of the specimen-induced phase shift, even when the corresponding intensity images are indistinguishable.

We illustrate this protocol in Appendix C for simple test potentials, where classically degenerate intensity patterns at focus give rise to clearly distinguishable ancilla signals. This example highlights how the quantum CTEM framework can access phase-sensitive observables beyond those available in conventional intensity-based imaging.

This example illustrates that the quantum CTEM framework enables access to coherent-state observables beyond those available from intensity-only detection, a qualitative advantage independent of computational scaling. Whether such phase-sensitive queries can be efficiently prepared and measured for realistic microscopy tasks remains an open question for future work.

#### 4. Comparison to state-of-the-art classical simulations

To contextualize the quantum approach, we compare runtime and scaling behavior to advanced classical CTEM simulation tools.

*a. Classical multislice codes.* Standard multislice on an  $N \times N$  grid requires  $O(N^2 \log N)$  operations per slice (two FFTs plus a pixel-wise phase multiplication) and  $O(N^2)$  memory. Modern GPU-accelerated implementations (e.g., ABTEM<sup>15</sup>, MULTEM<sup>44</sup>) achieve single-image runtimes of  $\sim 1\text{--}10$  seconds for  $N = 2048$  on high-end GPUs (NVIDIA A100, 40 TFLOPS).

For *parameter sweeps* varying accelerating voltage, defocus,  $C_3$ , specimen orientation, or thickness—the computational cost scales *linearly* with the number of parameter points. Exhaustive scans over  $10^3$  to  $10^6$  configurations are common in automated structure refinement and can require hours to days even on GPU clusters.

*b. PRISM and Fourier-space interpolation.* The PRISM algorithm<sup>14</sup> exploits Fourier-space interpolation to reduce the cost of STEM image simulation over many probe positions, achieving speedups of  $10^2$  to  $10^3$  for typical scan grids. However, PRISM is optimized for *scanning* geometries (varying probe position at fixed optics) and offers limited advantage for the *optical parameter sweeps* (varying  $\Delta f$ ,  $C_3$ , voltage) central to CTEM simulation. For such tasks, each parameter point still requires a full multislice propagation, and the classical cost remains  $O(N_{\text{param}} \times SN^2 \log N)$ .

#### c. Quantum circuit cost and measurement bottleneck.

The quantum circuit for a single CTEM image has gate depth  $O(n^2) = O(\log^2 N)$  and requires  $\sim 10^5$  to  $10^7$  non-Clifford gates for  $N = 128$  to 2048 (Table I). On a hypothetical fault-tolerant device with 1 GHz logical gate rate and  $10^{-9}$  error per gate, a single circuit execution would take  $\sim 0.1\text{--}10$  ms, competitive with or faster than classical FFT time.

However, the measurement bottleneck dominates for full-image output. Extracting all  $N^2$  pixel intensities with 1% relative error requires  $\sim 10^4$  shots per pixel, or  $\sim 10^8$  to  $10^9$  total circuit runs for  $N = 128$  to 2048 (Table I). At 1 ms per run, this corresponds to  $\sim 10^5$  to  $10^6$  seconds ( $\sim$  days), *orders of magnitude slower* than classical GPU codes for the same task.

*d. Regimes for potential quantum advantage.* Given the measurement overhead, quantum advantage for CTEM simulation requires tasks that *avoid full-image reconstruction*:

- 1. Fourier-space queries:** Estimating specific structure factors, Bragg peak intensities, or diffraction patterns via partial measurement in the QFT basis, requiring  $O(1)$  to  $O(\text{poly log } N)$  samples rather than  $O(N^2)$ .
- 2. Global image statistics:** Computing moments, symmetries, or other summary features that can be extracted via expectation values of few-qubit observables.
- 3. Phase-sensitive discriminators:** Using ancilla-assisted protocols (Sec. III 3, Appendix C) to distinguish structures with classically degenerate intensity signatures.
- 4. Extended physics beyond WPOA:** Simulating inelastic scattering, many-body correlations, or dynamical diffraction effects that scale exponentially for classical tensor-network methods but remain polynomial in system size for quantum circuits.

For the baseline WPOA imaging task studied here, i.e. producing a full classical image for human inspection or post-processing, no quantum advantage is expected over state-of-the-art classical codes. The value of the present framework lies in (i) establishing the correctness of the quantum mapping for controlled benchmarking, (ii) enabling phase-coherent measurements inaccessible classically, and (iii) providing a foundation for extensions to computationally hard regimes (thick specimens, inelastic processes, disorder averaging) where classical methods struggle.

## IV. DISCUSSION

### A. Relationship to classical unitary multislice

The quantum circuit structure, alternating diagonal operators in real and reciprocal space linked by QFTs, directly mirrors the unitary factorization of classical multislice.<sup>1,3</sup> Recent formal analyses<sup>45</sup> have shown that multislice, Bloch-wave, and scattering-matrix methods are mathematically equivalent unitary transformations. Our quantum algorithm is therefore

a direct implementation of this known unitary structure on a quantum register, not a fundamentally new physical model.

This equivalence clarifies the source of potential advantage: it cannot come from the propagation formalism itself (which is identical classically and quantumly) but must arise from either (i) *measurement strategies* that exploit coherent access to the wavefunction, or (ii) *extended physics* (inelastic, many-body) where classical unitary methods become intractable.

### B. Extensions toward full multislice and inelastic scattering

Full multislice for a specimen of  $S$  slices requires alternating specimen and propagation operators:

$$|\psi_{\text{out}}\rangle = \left[ U_{\text{QFT}}^\dagger U_P(z_s) U_{\text{QFT}} U_{\text{obj}}^{(s)} \right]^S |\psi_{\text{in}}\rangle, \quad (21)$$

with circuit depth  $O(S \times n^2)$ . For thick specimens ( $S \sim 100\text{--}1000$ ), this remains polynomial but increases gate counts to  $\sim 10^7$  to  $10^9$ , approaching or exceeding early fault-tolerant device capabilities.

Inelastic scattering (phonons, plasmons, core-loss excitations) requires adding ancilla qubits to track excitation states and implementing slice-dependent controlled unitaries. The state space grows exponentially in the number of allowed excitation channels, making exact classical simulation via state vectors intractable for more than  $\sim 20\text{--}30$  channels. Quantum circuits can represent such superpositions natively, but synthesizing realistic inelastic cross-sections (energy-loss probabilities, momentum transfers) into gate sequences remains an open challenge.

### C. Toward ab initio potentials and DFT integration

The present implementation uses independent-atom-model (IAM) potentials parameterized as sums of Gaussians.<sup>1</sup> Modern *ab initio* multislice incorporates density-functional-theory (DFT) charge densities via projector-augmented-wave (PAW) methods,<sup>46</sup> capturing charge transfer, bonding, and electrostatic screening absent in IAM.

Extending the quantum framework to PAW potentials requires replacing Gaussian evaluation with 3D spline interpolation of the DFT-derived  $V(\mathbf{r})$ . The arithmetic cost increases by  $\sim 10\times$  (due to higher-order polynomial fitting and denser sampling), but the circuit structure remains unchanged. Ancilla and T-gate counts scale proportionally; for typical PAW grids ( $\sim 0.1 \text{ \AA}$  spacing), we estimate  $\sim 10^6$  T-gates for  $N = 256$  (see Appendix B).

## V. CONCLUSION

We have presented a complete quantum algorithmic framework for conventional transmission electron microscopy (CTEM) image formation under the weak phase-object approximation, validated against classical multislice simulations

for a representative 2D material system across a comprehensive microscope parameter space. The quantum circuit implementation combines amplitude encoding, quantum Fourier transforms, and diagonal phase operators to map WPOA theory to fault-tolerant quantum gates, achieving quantitative agreement with classical references (RMSE  $< 1\%$ , SSIM  $> 0.99$ ) while requiring only  $O(\log N)$  qubits for an  $N \times N$  image grid.

Our resource analysis reveals that while the quantum circuit achieves polylogarithmic qubit count and gate depth, recovering a complete classical image requires  $O(N^2/\epsilon^2)$  measurements—a fundamental bottleneck for tasks demanding full pixel-by-pixel readout. Practical quantum advantage therefore lies not in replacing classical image simulation wholesale, but in three complementary regimes: (i) extracting global image properties (Fourier coefficients, symmetries, moments) with sub-quadratic sampling, (ii) accessing phase-sensitive observables via coherent measurement protocols inaccessible to classical intensity-only detection, and (iii) exploring high-dimensional parameter spaces where classical approaches face exponential cost.

The framework extends naturally beyond the present weak phase-object validation. Full multislice propagation requires iterating specimen-propagation-lens sequences over depth slices, raising questions of circuit depth and error accumulation that we address in ongoing work. Integration with quantum variational solvers and Hamiltonian simulation techniques may enable modeling of inelastic scattering, phonon coupling, and correlated electron dynamics in quantum materials—regimes where classical Hartree-Fock or TDDFT approaches become intractable. Extensions to quantum ptychography, coherent diffractive imaging, and time-resolved pump-probe microscopy follow the same QFT-based circuit primitives established here.

Near-term demonstrations on NISQ devices require problem-size reduction (coarse grids, limited aberrations) and error mitigation, but the logarithmic qubit scaling and modest gate counts ( $\sim 10^5$  to  $10^6$  T-gates) place early fault-tolerant implementations within reach of projected 2030s hardware. The convergence of these algorithmic developments with emerging experimental quantum electron optics<sup>20,21</sup> suggests that hybrid classical-quantum workflows—combining quantum simulation of phase-coherent dynamics with classical reconstruction and analysis—may offer the most practical path toward impact.

This work establishes quantum CTEM simulation as a physically grounded, experimentally validated application of quantum algorithms to computational microscopy, bridging electron optics, quantum information, and materials characterization under a unified framework.

## ACKNOWLEDGMENTS

This research was supported in part through the computational resources by the Quest high performance computing facility at Northwestern University, jointly supported by the Office of the Provost, Office for Research, and Northwest-

ern University Information Technology. We acknowledge the use of IBM Quantum services, specifically the Qiskit framework and `ibm_torino`, for this work<sup>47</sup>. The views expressed are those of the authors, and do not reflect the official policy or position of IBM or the IBM Quantum team. SDL thanks the support of the MRSEC program (NSF DMR-2308691) at the Northwestern Materials Research Center. SDL thanks the Materials Initiative for Comprehensive Research Opportunity (MICRO) program which benefited greatly from administrative and research support at MIT and Northwestern and from an unrestricted gift from the 3M Foundation (3M STEM and Skilled Trades Program).

## DATA AVAILABILITY STATEMENT

The data and code supporting the findings of this study are openly available in the QuScope examples repository at [https://github.com/QuScope/examples-applications/blob/main/notebooks/Quantum\\_ctem\\_paper\\_full\\_example.ipynb](https://github.com/QuScope/examples-applications/blob/main/notebooks/Quantum_ctem_paper_full_example.ipynb).<sup>42</sup> Example Jupyter notebook reproducing the MoS<sub>2</sub> validation results (Fig. 5, Appendix G), CTF parameter grids (Fig. 3, Appendix A), resource scaling analysis (Fig. 4, Table I), and IBM quantum hardware execution (Appendix F) are provided in the `examples/ctem/` directory. Classical reference simulations were performed using ABTEM v1.0.5<sup>15</sup>. Atomic scattering factor parameterizations follow Kirkland.<sup>1</sup> All quantum circuits were implemented in Qiskit v2.2.1.<sup>47</sup>

The data that support the findings of this study are openly available in [github.com/QuScope/QuScope](https://github.com/QuScope/QuScope).

## BIBLIOGRAPHY

- <sup>1</sup>E. J. Kirkland, *Advanced Computing in Electron Microscopy*, 3rd ed. (Springer, New York, 2020).
- <sup>2</sup>L. Reimer and H. Kohl, *Transmission Electron Microscopy: Physics of Image Formation*, 5th ed., Springer Series in Optical Sciences, Vol. 36 (Springer, New York, 2008).
- <sup>3</sup>J. M. Cowley and A. F. Moodie, “The Scattering of Electrons by Atoms and Crystals. I. A New Theoretical Approach,” *Acta Crystallographica* **10**, 609–619 (1957).
- <sup>4</sup>O. L. Krivanek, G. Corbin, N. Dellby, B. Elston, R. Keyse, M. Murfitt, C. Own, Z. Szilagyi, and J. Woodruff, “An electron microscope for the aberration-corrected era,” *Ultramicroscopy* **108**, 179–195 (2008).
- <sup>5</sup>M. Haider, S. Uhlemann, E. Schwan, H. Rose, B. Kabius, and K. Urban, “Electron microscopy image enhanced,” *Nature* **392**, 768–769 (1998).
- <sup>6</sup>M. A. O’Keefe, L. F. Allard, D. A. Blom, J. Chen, Z. Dai, B. Fultz, E. J. Kirkland, C. Kisielowski, C. Ma, M. R. McCartney, M. Pan, V. Radmilovic, A. Thust, J. Wagner, L. Wang, and Y. Zhang, “Sub-Ångstrom high-resolution transmission electron microscopy at 80–300 kV,” *Ultramicroscopy* (2001).
- <sup>7</sup>U. Dahmen, “Background, status and future of the transmission electron aberration-corrected microscope project,” *Philosophical Transactions of the Royal Society A* **367**, 3795–3808 (2009).
- <sup>8</sup>D. C. Bell, C. J. Russo, and G. Benner, “Sub-ångstrom low-voltage performance of a monochromated, aberration-corrected transmission electron microscope,” *Microscopy and Microanalysis* **16**, 386–392 (2010).
- <sup>9</sup>D. B. Williams and C. B. Carter, *Transmission Electron Microscopy: A Textbook for Materials Science*, 2nd ed. (Springer New York, NY, 2009).
- <sup>10</sup>M. Lentzen, “Contrast transfer and resolution limits for sub-angstrom high-resolution transmission electron microscopy,” *Microscopy and microanalysis* **14**, 16–26 (2008).
- <sup>11</sup>R. Kilaas, “Image simulation in high resolution transmission electron microscopy,” in *Electron Crystallography*, edited by D. L. Dorset, S. Hovmöller, and X. Zou (Springer Netherlands, Dordrecht, 1997) pp. 115–130.
- <sup>12</sup>C. Ophus, “Four-dimensional scanning transmission electron microscopy (4d-stem): From scanning nanodiffraction to ptychography and beyond,” *Microscopy and Microanalysis* **25**, 563–582 (2019).
- <sup>13</sup>“Machine learning in scanning transmission electron microscopy,” *Nature Reviews Methods Primers* (2022), 10.1038/s43586-022-00095-w.
- <sup>14</sup>C. Ophus, “A fast image simulation algorithm for scanning transmission electron microscopy,” *Advanced Structural and Chemical Imaging* **3**, 13 (2017).
- <sup>15</sup>J. Madsen and T. Susi, “The abTEM code: transmission electron microscopy from first principles,” *Open Research Europe* **1**, 24 (2021).
- <sup>16</sup>M. A. Nielsen and I. L. Chuang, *Quantum Computation and Quantum Information* (Cambridge University Press, 2010).
- <sup>17</sup>R. dos Reis, “Enhancing Microscopy Data Simulation and Analysis Using Quantum Algorithms,” *Microscopy and Microanalysis* **30** (2024), 10.1093/mam/ozae044.144.
- <sup>18</sup>Y. Wang, Y. Sun, and Z. Ding, “A quantum algorithm of multislice method,” *Results in Physics* **62**, 107834 (2024).
- <sup>19</sup>Y. Wang, Y. Sun, and Z. Ding, “An improved quantum algorithm of the multislice method,” *iScience* (2025), 10.1016/j.isci.2025.112165.
- <sup>20</sup>S. Löffler, T. Schachinger, P. Hartel, P.-H. Lu, R. E. Dunin-Borkowski, M. Obermair, M. Dries, D. Gerthsen, and P. Schattschneider, “A quantum logic gate for free electrons,” *Quantum* **7**, 1050 (2023).
- <sup>21</sup>T. Juffmann, S. A. Koppell, B. B. Klopf, C. Ophus, R. M. Glaeser, and M. A. Kasevich, “Multi-pass transmission electron microscopy,” *Scientific reports* **7**, 1699 (2017).
- <sup>22</sup>P. Kruit, R. G. Hobbs, C.-S. Kim, Y. Yang, V. R. Manfrinato, J. Hammer, S. Thomas, P. Weber, B. Klopfer, C. Kohstall, *et al.*, “Designs for a quantum electron microscope,” *Ultramicroscopy* **164**, 31–45 (2016).
- <sup>23</sup>C. Doberstein and P. Binev, “Lattice multislice algorithm for fast simulation of scanning transmission electron microscopy images,” *Microscopy and Microanalysis* **31**, ozae116 (2025), <https://academic.oup.com/mam/article-pdf/31/1/ozae116/61429031/ozae116.pdf>.
- <sup>24</sup>F. Hosokawa, T. Shinkawa, Y. Arai, and T. Sannomiya, “Benchmark test of accelerated multi-slice simulation by gpgpu,” *Ultramicroscopy* **158**, 56–64 (2015).
- <sup>25</sup>W. Van den Broek, X. Jiang, and C. Koch, “Fdes, a gpu-based multislice algorithm with increased efficiency of the computation of the projected potential,” *Ultramicroscopy* **158**, 89–97 (2015).
- <sup>26</sup>J. Barthel, “Time-efficient frozen phonon multislice calculations for image simulations in high-resolution stem,” in *15th European Microscopy Congress, Manchester* (2012).
- <sup>27</sup>V. Grillo and E. Rotunno, “Stem\_cell: A software tool for electron microscopy: Part i—simulations,” *Ultramicroscopy* **125**, 97–111 (2013).
- <sup>28</sup>L. J. Allen, S. Findlay, *et al.*, “Modelling the inelastic scattering of fast electrons,” *Ultramicroscopy* **151**, 11–22 (2015).
- <sup>29</sup>H. Okamoto, “Universal quantum electron microscopy: A small-scale quantum computing application with provable advantage,” (2022), arXiv:2209.04819 [quant-ph].
- <sup>30</sup>M. Schuld and F. Petruccione, *Machine Learning with Quantum Computers* (Springer, 2021).
- <sup>31</sup>R. F. Egerton *et al.*, *Physical principles of electron microscopy*, Vol. 56 (Springer, 2005).
- <sup>32</sup>H. H. Rose, “Prospects for aberration-free electron microscopy,” *Ultramicroscopy* **103**, 1–6 (2005).
- <sup>33</sup>J. Elferich, L. Kong, X. Zottig, and N. Grigorieff, “Ctffind5 provides improved insight into quality, tilt, and thickness of tem samples,” *Elife* **13**, RP97227 (2024).
- <sup>34</sup>S. Ashhab, “Quantum state preparation protocol for encoding classical data into the amplitudes of a quantum information processing register’s wave function,” *Phys. Rev. Research* **4**, 013091 (2022).
- <sup>35</sup>J. Gonzalez-Conde, T. W. Watts, P. Rodriguez-Grasa, and M. Sanz, “Efficient quantum amplitude encoding of polynomial functions,” *Quantum* **8**, 1297 (2024).
- <sup>36</sup>B. G. Thomas and B. G. Mendis, “Parameterized absorptive electron scat-

tering factors,” *Acta Crystallographica Section A* **80**, a00110 (2024).

<sup>37</sup>A. G. Fowler, M. Mariantoni, J. M. Martinis, and A. N. Cleland, “Surface codes: Towards practical large-scale quantum computation,” *Physical Review A* **86**, 032324 (2012).

<sup>38</sup>S. Bravyi and A. Kitaev, “Universal quantum computation with ideal clifford gates and noisy ancillas,” *Physical Review A* **71** (2005).

<sup>39</sup>D. Litinski, “Magic state distillation: Not as costly as you think,” *Quantum* **3**, 205 (2019).

<sup>40</sup>S. Aaronson, “Read the fine print,” *Nature Physics* **11**, 291–293 (2015).

<sup>41</sup>M. Schuld and N. Killoran, “Quantum machine learning in feature hilbert spaces,” *Physical Review Letters* **122**, 040504 (2019).

<sup>42</sup>S. D. Lam and R. dos Reis, “Quscope: Quantum algorithms for microscopy,” (2025), GitHub repository.

<sup>43</sup>R. M. Glaeser, “Invited review article: Methods for imaging weak-phase objects in electron microscopy,” *Review of Scientific Instruments* **84** (2013).

<sup>44</sup>I. L. Hoyos, J. Verbeeck, and S. Van Aert, “Recent advances of the open source multem program to provide accurate and fast electron microscopy simulations,” *Microscopy and Microanalysis* **23**, 206–207 (2017).

<sup>45</sup>A. Bangun, O. Melnyk, and B. März, “Eigenstructure analysis of bloch wave and multislice matrix formulations for dynamical scattering in transmission electron microscopy,” arXiv preprint arXiv:2412.21119 (2024).

<sup>46</sup>T. Susi *et al.*, “Ab initio description of bonding for transmission electron microscopy,” *Ultramicroscopy* (2021), arXiv:2010.07145, arXiv:2010.07145 [cond-mat.mtrl-sci].

<sup>47</sup>A. Javadi-Abhari, M. Treinish, K. Krsulich, C. J. Wood, J. Lishman, J. Gacon, S. Martiel, P. D. Nation, L. S. Bishop, A. W. Cross, B. R. Johnson, and J. M. Gambetta, “Quantum computing with Qiskit,” (2024), arXiv:2405.08810 [quant-ph].

<sup>48</sup>V. Shende, S. S. Bullock, and I. L. Markov, “Synthesis of quantum-logic circuits,” *Ieee Transactions on Computer-Aided Design of Integrated Circuits and Systems* **25**, 1000–1010 (2006).

<sup>49</sup>T. Häner, M. Roetteler, and K. M. Svore, “Factoring using 2n+2 qubits with toffoli based modular multiplication,” arXiv preprint arXiv:1611.07995 (2016).

## Appendix A: Contrast Transfer Function with Coherence Envelopes

This appendix provides detailed validation of the quantum circuit implementation of objective-lens aberrations via comparison of computed contrast transfer functions (CTF) to analytical theory across a range of accelerating voltages, defocus values, and spherical aberration coefficients.

### 1. Coherent CTF and envelope functions

The idealized *coherent* contrast transfer function for an axially symmetric lens is given by Eq. (8) in the main text, with the phase shift  $\chi(k)$  [Eq. (7)] including defocus  $\Delta f$  and spherical aberration  $C_3$ .

In practice, finite source size (spatial coherence) and energy spread (temporal/chromatic coherence) introduce damping envelope functions that suppress high spatial frequencies:<sup>1,2</sup>

a. *Spatial coherence envelope.* Finite effective source size  $\Delta$  (determined by electron source brightness and condenser demagnification) produces a Gaussian envelope:

$$E_s(k) = \exp\left(-\frac{\pi^2 \Delta^2 \lambda^2 k^4}{4 \ln 2}\right). \quad (\text{A1})$$

For a field-emission gun (FEG) with typical  $\Delta \sim 5\text{--}10 \text{ nm}$  (reduced source size at the specimen),  $E_s$  damps contributions beyond  $k \sim 0.5\text{--}0.7 \text{ \AA}^{-1}$ .

b. *Chromatic coherence envelope.* Energy spread  $\Delta E$  and chromatic aberration coefficient  $C_c$  introduce an additional envelope:

$$E_c(k) = \exp\left(-\frac{\pi^2 C_c^2 (\Delta E/E_0)^2 k^4}{2 \ln 2}\right). \quad (\text{A2})$$

For a FEG at 80 kV with  $\Delta E \sim 0.3 \text{ eV}$  and  $C_c \sim 1.3 \text{ mm}$ ,  $E_c$  provides similar damping at  $k \sim 0.6\text{--}0.8 \text{ \AA}^{-1}$ .

c. *Effective CTF.* The experimentally observable transfer function is the product:

$$\text{CTF}_{\text{eff}}(k) = E_s(k) E_c(k) \sin[\chi(k)]. \quad (\text{A3})$$

The *information limit*  $k_{\text{info}}$  is conventionally defined where  $\text{CTF}_{\text{eff}}$  drops to  $1/e$  of its maximum, typically  $k_{\text{info}} \sim 0.5\text{--}0.8 \text{ \AA}^{-1}$  for a modern FEG-TEM, corresponding to a real-space resolution of  $\sim 1.2\text{--}2.0 \text{ \AA}$ .<sup>1,2</sup>

### 2. Quantum circuit validation: Coherent CTF

In the present quantum CTEM implementation, we compute the *coherent* CTF [Eq. (8)] to validate the gate-level realization of the lens phase operator  $U_\chi$  against analytical expressions for  $\chi(k)$ . Partial coherence and detector response are *not* included in the current circuit but can be incorporated via:

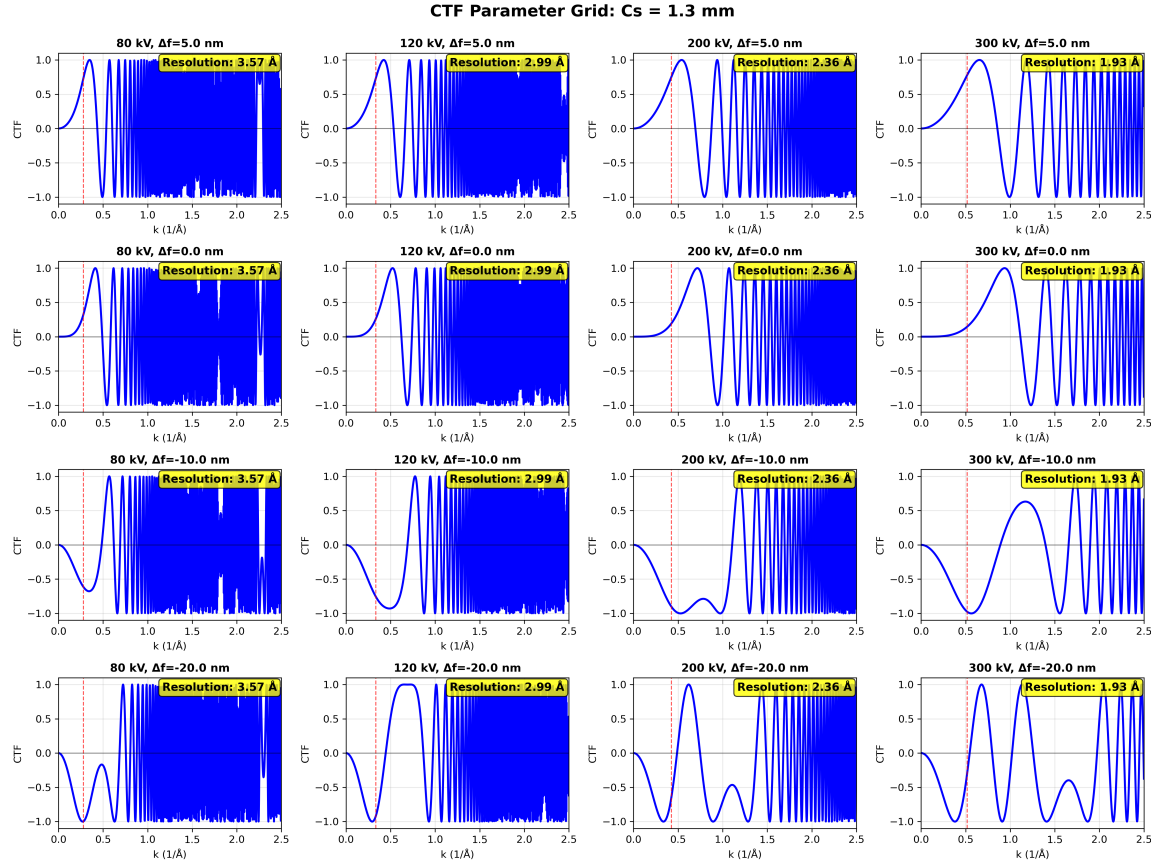


FIG. A1. Quantum-computed CTF parameter grid spanning four accelerating voltages (80, 120, 200, 300 kV) and four defocus values (+5.0, 0.0, -10.0, -20.0 nm) at fixed spherical aberration  $C_3 = 1.3$  mm. Each panel shows the CTF versus spatial frequency  $k$ . The red dashed line marks the resolution limit  $k_{\text{res}} = 1/d_{\text{res}}$  based on the idealized coherent CTF. Resolution improves systematically with increasing accelerating voltage (left to right: 3.57 Å at 80 kV to 1.93 Å at 300 kV at Scherzer defocus), reflecting the decrease in electron wavelength  $\lambda \propto 1/\sqrt{V_{\text{acc}}}$ . At Gaussian focus ( $\Delta f = 0.0$  nm, second row), phase contrast vanishes at low spatial frequencies for all voltages. Underfocus ( $\Delta f < 0$ ) generates positive phase contrast with characteristic CTF envelope expansion at larger defocus values (bottom row). This grid validates the quantum algorithm's faithful reproduction of standard microscope transfer-function behavior across the experimentally relevant parameter space.<sup>1</sup>

1. **Ensemble averaging:** Running multiple quantum circuits with statistically sampled defocus/energy variations and incoherently summing intensity outputs (classical post-processing),
2. **Mixed-state encoding:** Representing partial coherence as a density matrix  $\rho = \sum_i p_i |\psi_i\rangle\langle\psi_i|$  and evolving via purification or Monte Carlo sampling (exponential overhead in coherence parameters),
3. **Detector convolution:** Applying a detector modulation transfer function (MTF) as a classical Fourier-space filter after quantum measurement.

For the CTF validation presented here, we focus on the coherent limit to isolate errors in the  $U_\chi$  gate synthesis from environmental or instrumental effects. Extension to realistic partial coherence is discussed in Sec. IV.

This appendix confirms that the quantum CTEM circuit correctly implements the optical transfer theory underpinning phase-contrast imaging, establishing confidence in the subsequent image formation results (Sec. III).

## Appendix B: Diagonal Operator Synthesis and Arithmetic Circuits

This appendix provides explicit circuit constructions and resource estimates for implementing the diagonal specimen operator  $U_{\text{obj}}$  and lens aberration operator  $U_\chi$  via arithmetic evaluation of the phase functions  $\sigma V_{ij}$  and  $\chi(k)$ .

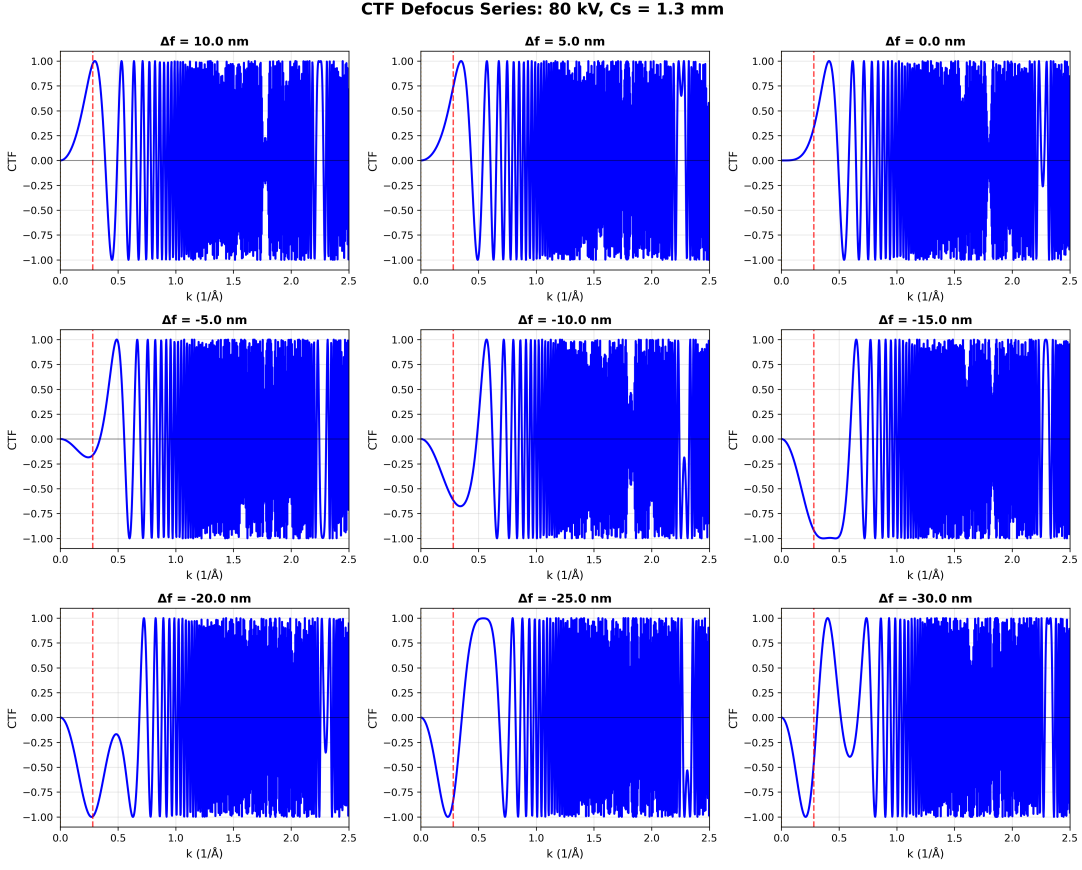


FIG. A2. Through-focus series of quantum-computed CTF at 80 kV with fixed spherical aberration  $C_3 = 1.3$  mm. Nine defocus values are shown ranging from  $\Delta f = +10.0$  nm (overfocus) through  $\Delta f = 0.0$  nm (Gaussian focus) to  $\Delta f = -30.0$  nm (underfocus). The red dashed line marks the resolution limit  $k_{\text{res}} = 1/d_{\text{res}}$  based on the idealized coherent CTF. At Gaussian focus ( $\Delta f = 0.0$  nm), the CTF approaches zero at low spatial frequencies, producing negligible phase contrast. Underfocus ( $\Delta f < 0$ ) generates positive phase contrast (bright atoms), while overfocus ( $\Delta f > 0$ ) produces inverted contrast, with the CTF envelope and zero positions evolving systematically with defocus as predicted by Eq. 7.<sup>1</sup>

### 1. Specimen operator $U_{\text{obj}}$ : Atomic potential evaluation

The projected potential at grid point  $(i, j)$  is computed as a superposition of atomic contributions:

$$V_{ij} = \sum_{a=1}^{N_{\text{atoms}}} \sum_{m=1}^M a_m^{(a)} \exp\left(-\frac{\pi r_{ij,a}^2}{b_m^{(a)}}\right), \quad (\text{B1})$$

where  $r_{ij,a}^2 = (x_i - x_a)^2 + (y_j - y_a)^2$  is the squared distance from grid point  $(i, j)$  to atom  $a$  at position  $(x_a, y_a)$ , and  $\{a_m^{(a)}, b_m^{(a)}\}$  are the Kirkland parameterization coefficients for atomic species  $Z(a)$ .<sup>1</sup>

The diagonal unitary is

$$U_{\text{obj}} = \sum_{i,j=0}^{N-1} e^{i\sigma V_{ij}} |i, j\rangle \langle i, j|. \quad (\text{B2})$$

#### a. Circuit architecture

We implement  $U_{\text{obj}}$  via the following steps:

a. *Step 1: Position register encoding.* The computational basis state  $|i, j\rangle$  encodes the grid coordinates in two  $n/2$ -qubit registers ( $n = 2\log_2 N$ ), with  $i, j \in [0, N-1]$ . These are interpreted as fixed-point binary numbers representing physical coordinates:

$$x_i = x_{\min} + i \cdot \Delta x, \quad y_j = y_{\min} + j \cdot \Delta y, \quad (\text{B3})$$

where  $\Delta x = \Delta y = L/N$  is the pixel size and  $L$  is the simulation box dimension.

b. *Step 2: Distance computation.* For each atom  $a$ , compute the squared distance  $r_{ij,a}^2$  using binary arithmetic on the position registers:

1. Subtract atomic coordinates:  $\Delta x_a = x_i - x_a$ ,  $\Delta y_a = y_j - y_a$  (requires  $n/2$ -bit subtraction,  $\sim 2n$  gates via ripple-carry or  $\sim \log n$  depth with carry-lookahead).
2. Square each difference:  $\Delta x_a^2, \Delta y_a^2$  (requires  $n/2$ -bit multiplication,  $\sim n^2$  gates or  $\sim n \log n$  with Karatsuba).
3. Sum:  $r_{ij,a}^2 = \Delta x_a^2 + \Delta y_a^2$  ( $n$ -bit addition,  $\sim 2n$  gates).

Total cost per atom:  $O(n^2)$  gates (or  $O(n \log n)$  with optimized multipliers), depth  $O(\log n)$  to  $O(n)$  depending on parallelization.

c. *Step 3: Gaussian evaluation.* Evaluate  $\exp(-\pi r_{ij,a}^2/b_m)$  for each Gaussian term  $m$ . We approximate the exponential via a degree- $d$  polynomial (Chebyshev, Taylor, or minimax) over the range  $r^2 \in [0, r_{\max}^2]$ :

$$\exp(-\pi r^2/b_m) \approx \sum_{k=0}^d c_k \left( \frac{r^2}{r_{\max}^2} \right)^k. \quad (\text{B4})$$

For target accuracy  $\varepsilon \sim 10^{-6}$  over the atomic column region ( $r_{\max} \sim 2 \text{ \AA}$ ),  $d \approx 8\text{--}12$  suffices. Evaluating the polynomial requires:

- $d$  multiplications (each  $\sim n \log n$  gates with Karatsuba),
- $d$  additions (each  $\sim 2n$  gates),
- One division by  $r_{\max}^2$  (amortized via precomputed scaling).

Cost per Gaussian:  $\sim d \times n \log n \approx 100n$  to  $500n$  gates, or equivalently  $\sim 10^3$  to  $10^4$  T-gates after compilation to Clifford+T (assuming each rotation  $R_z(\theta)$  costs  $\sim 50$  T-gates at  $10^{-9}$  precision).

Alternative using CORDIC: Exponential evaluation via coordinate rotation digital computer (CORDIC) iterations requires  $\sim p$  iterations for  $p$ -bit precision, with  $\sim 4p$  gates per iteration (shifts, additions, controlled rotations). For  $p = 20\text{--}30$  bits, cost is  $\sim 10^2$  to  $10^3$  gates per exponential.

d. *Step 4: Accumulation.* Sum the contributions from all Gaussians across all atoms into a fixed-point accumulator register  $|V_{ij}\rangle$  (width  $p \sim 20\text{--}30$  bits):

$$V_{ij} = \sum_{a=1}^{N_{\text{atoms}}} \sum_{m=1}^M a_m^{(a)} \exp(-\pi r_{ij,a}^2/b_m^{(a)}). \quad (\text{B5})$$

Each accumulation step is a  $p$ -bit addition; total cost  $O(N_{\text{atoms}} \times M \times p)$  gates.

e. *Step 5: Phase kickback.* Apply the phase rotation  $e^{i\sigma V_{ij}}$  controlled on the position register  $|i, j\rangle$  and the computed potential  $|V_{ij}\rangle$  via a controlled- $R_z$  gate:

$$R_z(\sigma V_{ij})|i, j\rangle = e^{i\sigma V_{ij}/2}|i, j\rangle. \quad (\text{B6})$$

This requires a  $p$ -bit controlled phase gate, synthesized into  $\sim 50p$  T-gates via standard rotation decompositions.<sup>16</sup>

f. *Step 6: Uncomputation.* Reverse Steps 2–4 to uncompute the ancilla registers (distance, Gaussian values, accumulator), leaving only the phase imprinted on  $|i, j\rangle$ . This doubles the gate count but keeps ancilla reusable.

**b. Resource summary for  $U_{obj}$**

For a MoS<sub>2</sub> 3 × 2 supercell with  $N_{\text{atoms}} = 18$  and  $M = 5$  Gaussians per species:

• **Ancilla qubits:**

- Position arithmetic (subtraction, squaring):  $\sim 2n$  qubits
- Gaussian evaluation:  $\sim 2p$  qubits per term (input/output registers)
- Accumulator:  $p$  qubits
- Total:  $\sim 30\text{--}50$  ancilla qubits for  $n = 14$  (128×128 grid),  $p = 24$  bits

• **Gate count:**

- Distance computation:  $\sim n^2 \times N_{\text{atoms}} \approx 14^2 \times 18 \approx 3500$  two-qubit gates
- Gaussian evaluation:  $\sim 10^4$  gates/term  $\times (N_{\text{atoms}} \times M) \approx 10^4 \times 90 = 9 \times 10^5$  gates
- Accumulation & phase kickback:  $\sim 10^3$  gates
- Uncomputation (doubling): factor of 2
- **Total (forward+reverse):**  $\sim 2 \times 10^6$  gates, of which  $\sim 10^5$  are non-Clifford (T-gates) after optimization

• **Circuit depth:** With parallelization over independent atoms and pipelined arithmetic, depth  $\sim O(N_{\text{atoms}} \times n \log n) \approx 10^3$  to  $10^4$  layers (gate depth, not T-depth).

Scaling to larger grids (256×256,  $n = 16$ ) or denser supercells ( $N_{\text{atoms}} \sim 50\text{--}100$ ) increases gate counts proportionally:  $\sim 10^6$  T-gates for  $N = 256$ ,  $\sim 10^7$  for  $N = 2048$ .

**2. Lens aberration operator  $U_\chi$**

The lens phase in momentum space is

$$\chi(k) = \pi\lambda\Delta f k^2 + \frac{1}{2}\pi\lambda^3 C_3 k^4 + \frac{1}{3}\pi\lambda^5 C_5 k^6 + \dots, \quad (\text{B7})$$

where  $k^2 = k_x^2 + k_y^2$ . For typical CTEM imaging, truncation at  $C_3$  (spherical aberration) suffices; higher-order terms ( $C_5$ , chromatic aberration) follow the same circuit structure.

**a. Circuit construction**

- a. *Step 1: Momentum register.* After the QFT, the state is in the momentum basis  $|k_x, k_y\rangle$ , with  $k_x, k_y \in [-N/2, N/2)$  encoded in  $n/2$ -qubit two's-complement registers.
- b. *Step 2: Squared momentum.* Compute  $k_x^2$ ,  $k_y^2$ , and  $k^2 = k_x^2 + k_y^2$  using  $n/2$ -bit squaring circuits (cost  $\sim n^2$  gates per square, depth  $O(n)$ ).
- c. *Step 3: Quartic term.* Compute  $k^4 = (k^2)^2$  (one additional squaring,  $\sim n^2$  gates).
- d. *Step 4: Phase evaluation.* Evaluate the polynomial

$$\chi(k) = a_2 k^2 + a_4 k^4, \quad (\text{B8})$$

where  $a_2 = \pi\lambda\Delta f$  and  $a_4 = \pi\lambda^3 C_3/2$  are precomputed classical constants. This requires:

- Two multiplications:  $a_2 k^2$ ,  $a_4 k^4$  (each  $\sim n \log n$  gates),
- One addition:  $\chi = a_2 k^2 + a_4 k^4$  ( $\sim 2n$  gates).

- e. *Step 5: Phase kickback and uncomputation.* Apply  $R_z(\chi)$  controlled on  $|k_x, k_y\rangle$  (cost  $\sim 50p$  T-gates for  $p$ -bit precision), then reverse Steps 2–4 to free ancilla.

*b. Resource summary for  $U_\chi$*

- **Ancilla qubits:**  $\sim 2p$  for intermediate  $k^2, k^4$  registers; typically  $\sim 20\text{--}30$  qubits.
- **Gate count:**
  - Three squarings:  $3 \times n^2 \approx 600$  gates for  $n = 14$
  - Polynomial evaluation:  $\sim n \log n \approx 50$  gates
  - Phase kickback:  $\sim 50p \approx 1200$  T-gates
  - Uncomputation: factor of 2
  - **Total:**  $\sim 10^3$  to  $10^4$  gates,  $\sim 2 \times 10^3$  T-gates
- **Depth:**  $O(n)$  for sequential squaring,  $O(\log n)$  with parallel multipliers.

The lens operator is *significantly cheaper* than the specimen operator because  $\chi(k)$  is a smooth, low-order polynomial depending only on  $k^2$  and  $k^4$ , whereas  $V_{ij}$  requires evaluating  $N_{\text{atoms}} \times M$  exponential terms.

### 3. Total resource budget

For a complete CTEM circuit on a 128×128 grid ( $n = 14$ ):

TABLE A1. Detailed resource breakdown for quantum CTEM circuit.

Component	Qubits	Total gates	T-gates	Depth
State preparation (Hadamards)	14	14	0	1
$U_{\text{obj}}$ (specimen)	14 + 40	$2 \times 10^6$	$1 \times 10^5$	$10^4$
QFT (forward)	14 + 2	$\sim 200$	$\sim 100$	$\sim 50$
$U_P$ (propagation)	14 + 20	$10^4$	$2 \times 10^3$	100
$U_\chi$ (lens)	14 + 20	$10^4$	$2 \times 10^3$	100
QFT <sup>†</sup> (inverse)	14 + 2	$\sim 200$	$\sim 100$	$\sim 50$
<b>Total</b>	<b>14 data + 40 ancilla</b>	<b><math>\sim 2 \times 10^6</math></b>	<b><math>\sim 1 \times 10^5</math></b>	<b><math>\sim 10^4</math></b>

Scaling to 256×256 ( $n = 16$ ) or 2048×2048 ( $n = 22$ ):

- Data qubits scale as  $2 \log_2 N$ : 16 and 22, respectively.
- Ancilla count is roughly constant ( $\sim 30\text{--}50$ ) for fixed precision  $p$  and number of atoms  $N_{\text{atoms}}$ .
- Gate counts scale as  $O(N_{\text{atoms}} \times M \times n^2)$  for  $U_{\text{obj}}$  and  $O(n^2)$  for QFT/lens:  $\sim 10^6$  T-gates for  $N = 256$ ,  $\sim 10^7$  for  $N = 2048$  (Table I, main text).

### 4. Extensions and optimizations

*a. Ab initio (PAW/DFT) potentials.* Replacing Kirkland Gaussians with DFT-derived charge densities requires 3D spline interpolation to evaluate  $V(\mathbf{r})$  from a fine-grid ( $\sim 0.1$  Å spacing) lookup table. Cubic spline evaluation involves:

- Finding the enclosing grid cell (binary search or direct indexing,  $O(\log N_{\text{grid}})$  comparisons),
- Evaluating a piecewise cubic polynomial (similar cost to Gaussian evaluation,  $\sim 10^4$  gates per lookup),
- Interpolating in 3D (requires  $2^3 = 8$  lookups per atom).

Estimated cost increase:  $\sim 5\text{--}10 \times$  over IAM Gaussians, yielding  $\sim 10^6$  T-gates for  $N = 256$ ,  $\sim 10^7$  for  $N = 2048$ . This remains polynomial in  $n$  and  $N_{\text{atoms}}$ , preserving asymptotic scaling.

b. *Arithmetic circuit optimizations.*

- **Approximate computing:** Reducing precision from  $p = 24$  to  $p = 16$  bits can halve T-counts with negligible impact on image fidelity for WPOA (phase errors  $< 10^{-4}$  rad).
- **Lookup tables:** For repeated potential evaluations (e.g., identical atoms), memoization or QROM can reduce exponential evaluations to  $O(\log N_{\text{table}})$  lookups, saving  $\sim 30\%$  gates in dense supercells.
- **Parallel arithmetic:** Exploiting independent atom computations with  $O(\log N_{\text{atoms}})$  depth via tree reduction can reduce circuit depth by  $10\text{--}100\times$  on hardware with high connectivity.

## 5. Comparison to "oracle" assumptions in prior work

Previous quantum multislice proposals<sup>18,19</sup> assume the specimen phase operator  $U_{\text{obj}}$  is implemented via an abstract "oracle" with unspecified cost, effectively treating  $V_{ij}$  as a black-box function. Our explicit arithmetic construction demonstrates that:

1. For physically realistic potentials (IAM Gaussians or PAW splines),  $U_{\text{obj}}$  can be synthesized with polynomial overhead in  $n$  and  $N_{\text{atoms}}$ , validating the oracle assumption *in this regime*.
2. The constant factors are non-trivial:  $\sim 10^5$  T-gates per image for small grids, increasing to  $\sim 10^6\text{--}10^7$  for production-scale simulations.
3. Arbitrary or adversarially chosen potentials (e.g., dense high-frequency noise, discontinuities) could require exponentially-sized data loading, breaking polynomial scaling. The smoothness and locality of physical atomic potentials are *essential* to efficient synthesis.

This analysis clarifies the computational assumptions underlying quantum CTEM simulation and provides concrete targets for experimental validation on near-term fault-tolerant devices.

## Appendix C: Ancilla-assisted phase discrimination

In this Appendix we provide numerical examples supporting the ancilla-assisted phase discrimination protocol introduced in Sec. III 3. To quantify the phase-sensitive capability of the ancilla-assisted protocol introduced in Sec. III 3, we evaluate the ancilla expectation value in the  $Y$  basis,  $\langle Y_a \rangle$ , for several test potentials on a  $16 \times 16$  grid at 80 kV and focus. For each scenario we consider a conjugate pair of projected potentials  $V(\mathbf{r}_\perp)$  and  $-V(\mathbf{r}_\perp)$ , as well as a control case of two independent random potentials.

Table A2 summarizes the results. Gaussian phase gratings with amplitudes  $A = 1000, 3000$ , and  $5000$  (arbitrary units) yield large, antisymmetric signals, with  $\langle Y_a \rangle(+V) \approx -\langle Y_a \rangle(-V)$  and  $|\Delta\langle Y_a \rangle|$  ranging from 0.36 to 0.63. Random conjugate pairs produce smaller but still clearly resolvable signals, while two independent random potentials give a near-zero discrimination signal  $|\Delta\langle Y_a \rangle| \approx 0.01$ . In all cases, the corresponding CTEM intensity images at focus are numerically indistinguishable within the accuracy of the simulation (not shown), confirming that the ancilla measurement accesses phase information that is inaccessible to intensity-only detection.

TABLE A2. Ancilla-based phase discrimination in the  $Y$  basis for conjugate potential pairs  $V$  and  $-V$  and for two independent random potentials on a  $16 \times 16$  grid at 80 kV and focus. The quantity  $\Delta\langle Y_a \rangle = \langle Y_a \rangle(+V) - \langle Y_a \rangle(-V)$  provides a phase-sensitive discrimination signal, which is large for  $\pm V$  pairs and nearly vanishing for independent potentials.

Scenario	$\langle Y_a \rangle(+V)$	$\langle Y_a \rangle(-V)$	$\Delta\langle Y_a \rangle$
Gaussian ( $A = 1000$ )	-0.1785	+0.1785	-0.3571
Gaussian ( $A = 3000$ )	-0.3158	+0.3158	-0.6315
Gaussian ( $A = 5000$ )	-0.2474	+0.2474	-0.4947
Random #1	-0.0150	+0.0150	-0.0299
Random #2	+0.0548	-0.0548	+0.1096
Random #3	+0.0059	-0.0059	+0.0118
Independent random	+0.0016	-0.0108	+0.0124

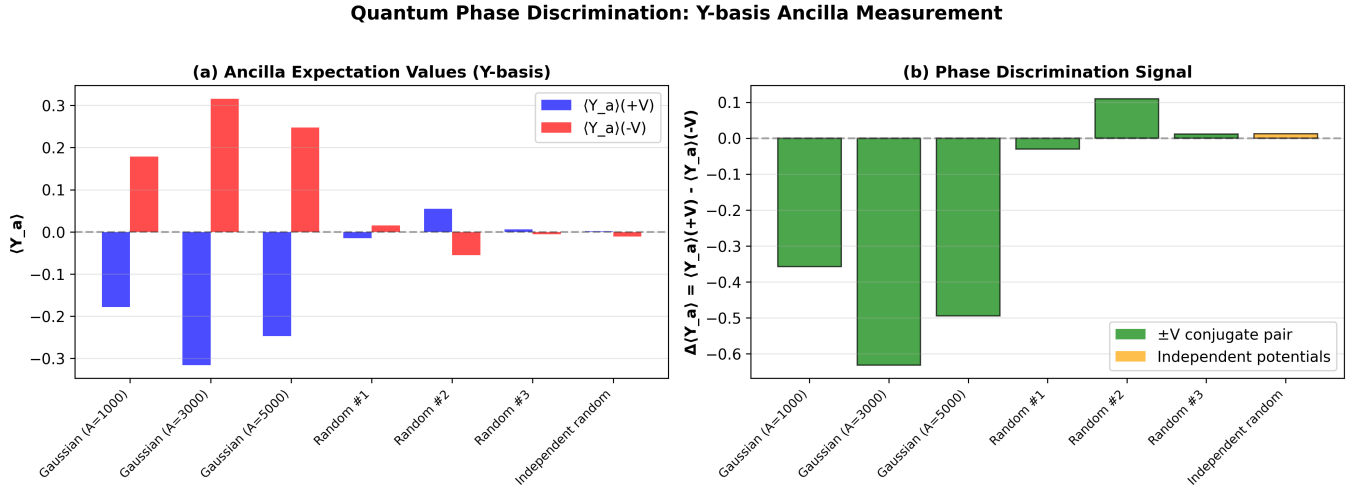


FIG. A3. Ancilla-based phase discrimination in the  $Y$  basis for conjugate potential pairs  $V$  and  $-V$  on a  $16 \times 16$  grid at 80 kV and focus. (a) Ancilla expectation values  $\langle Y_a \rangle$  for  $+\sigma V$  (blue) and  $-\sigma V$  (red). For Gaussian phase gratings (left),  $\langle Y_a \rangle(+V)$  and  $\langle Y_a \rangle(-V)$  have opposite signs and large magnitude, while random conjugate pairs produce smaller but still resolvable signals. (b) Discrimination signal  $\Delta\langle Y_a \rangle = \langle Y_a \rangle(+V) - \langle Y_a \rangle(-V)$ , highlighting the strong response for  $\pm V$  conjugate pairs (green) and the near-zero response for two independent random potentials (orange). The corresponding CTEM intensities at focus are numerically indistinguishable for each  $\pm V$  pair, demonstrating that the ancilla measurement accesses phase information that is invisible to intensity-only detection.

#### Appendix D: Algorithmic Complexity and Quantum Advantage

In this Appendix we summarize the asymptotic resource requirements of the quantum CTEM algorithm and contrast them with classical multislice simulations on an  $N \times N$  grid.

##### 1. Classical multislice scaling

Classical CTEM multislice calculations require storing  $O(N^2)$  complex amplitudes per slice and performing at least two FFTs per slice, each with  $O(N^2 \log N)$  arithmetic operations. For  $S$  slices, the total runtime can be written as

$$T_{\text{classical}} = O(SN^2 \log N), \quad (\text{D1})$$

with a memory footprint of  $O(N^2)$ . These costs become prohibitive for  $N \gtrsim 2048$  and for large parameter sweeps over accelerating voltage, defocus, aberrations, thickness, and specimen configurations.

##### 2. Quantum CTEM scaling

In the quantum formulation, the discretized wavefield on an  $N \times N$  grid is amplitude-encoded into an  $n_x = \log_2 N$ -qubit register for  $x$  and an  $n_y = \log_2 N$ -qubit register for  $y$ , for a total of

$$n = n_x + n_y = 2 \log_2 N \quad (\text{D2})$$

qubits.

The two-dimensional QFT used for free-space propagation and lens aberrations decomposes as  $U_{\text{QFT}} = \text{QFT}_x \otimes \text{QFT}_y$ , where each one-dimensional QFT layer requires  $O(n^2)$  one- and two-qubit gates and depth  $O(n^2)$ .

The specimen and lens operators are diagonal in the position and momentum bases, respectively, and can be synthesized using arithmetic circuits that evaluate the smooth phase functions  $\sigma V_{ij}$  and  $\chi(k)$  with  $O(\text{poly}(n))$  T-gates. Under the weak phase object approximation and for low-order aberration polynomials, the overall circuit depth for a single CTEM image therefore scales as

$$D_{\text{quantum}} = O(n^2) + O(\text{poly}(n)) = O((\log N)^p), \quad (\text{D3})$$

for some constant  $p$ , while the number of qubits scales as  $O(\log N)$ .

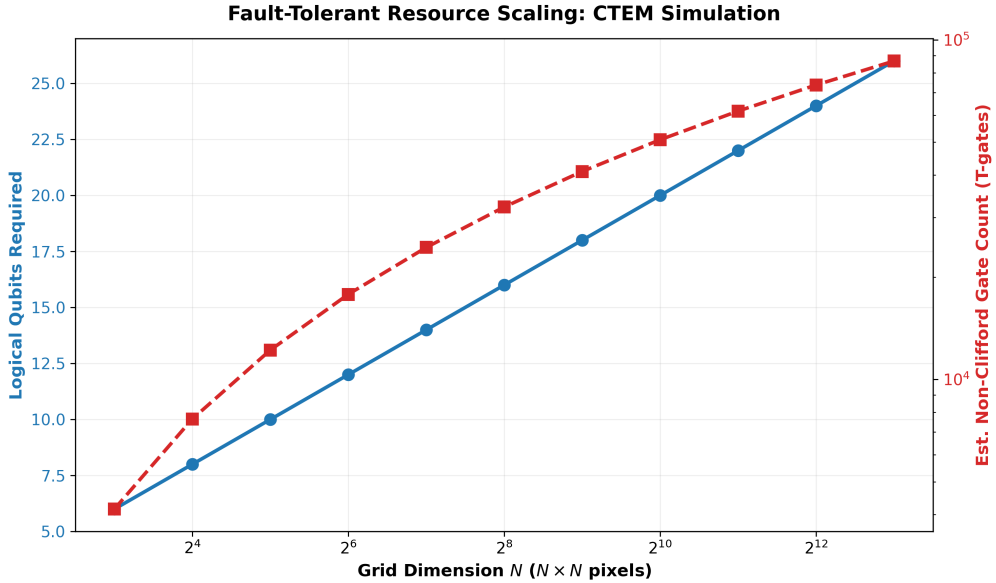


FIG. A4. Fault-tolerant resource scaling for the quantum CTEM circuit. The left axis shows the number of logical qubits as a function of grid dimension  $N$  (blue circles), while the right axis shows the estimated non-Clifford (T) gate count based on the arithmetic model described in Sec. D 3 (red squares, logarithmic scale).

### 3. Fault-tolerant resource estimation

To connect the asymptotic scaling to concrete fault-tolerant costs, we estimate non-Clifford (T) gate counts for representative grid sizes using a combination of prototype circuit transpilation and simple arithmetic models. Figure A4 summarizes the resulting scaling of logical qubits and T-gates for grids from  $4 \times 4$  up to  $2048 \times 2048$ .

For a small  $8 \times 8$  grid (corresponding to  $n = 6$  qubits), we construct the full CTEM circuit using QUSCOPE and QISKit, and transpile it to a  $\{\text{CX}, U_3\}$  basis with moderate optimization. Counting single-qubit rotations and assuming a synthesis cost of approximately 50 T-gates per arbitrary rotation (sufficient for target phase precisions near  $10^{-10}$ ), we obtain an effective T-count of order  $10^4$  for the prototype implementation, dominated by the QFT and diagonal phase decompositions.

To extrapolate to larger grids and a more arithmetic-friendly implementation, we approximate the T-cost as follows. For an  $N \times N$  grid encoded in  $n = 2\log_2 N$  qubits, each one-dimensional QFT layer uses  $O(n^2)$  controlled-phase gates, which we model as  $(n(n-1))$  controlled-phase operations, with each synthesized using  $\mathcal{O}(50)$  T-gates. The CTF and specimen phase operators are implemented as diagonal unitaries whose phases are evaluated using simple arithmetic on the binary indices  $(i, j)$  and  $(k_x, k_y)$ ; for the quadratic and quartic terms  $k^2$  and  $k^4$  entering the Fresnel and aberration phases, we model this as roughly  $4n^2$  Toffoli gates, with each Toffoli decomposed into 4 T-gates. Summing over two QFT layers and two diagonal operators yields an estimated non-Clifford cost

$$T_{\text{FT}}(N) \approx 2T_{\text{QFT}}(n) + 2T_{\text{diag}}(n), \quad (\text{D4})$$

where  $T_{\text{QFT}}(n) \sim 50n(n-1)$  and  $T_{\text{diag}}(n) \sim 16n^2$  in our simple model.

Using this estimate, we obtain the illustrative fault-tolerant resource targets listed in Table A1, with logical qubit counts growing only as  $2\log_2 N$ .

These values are consistent with the trend shown in Figure A4, which plots both the logical qubit requirement and the estimated T-gate count as functions of grid dimension. We emphasize that these numbers are order-of-magnitude estimates: they neglect constant factors from error-correction overhead, assume efficient arithmetic implementations for phase evaluation, and focus on the dominant QFT and diagonal-phase layers. Nevertheless, they provide a useful bridge between the abstract complexity discussion and concrete fault-tolerant resource budgets for early logical devices with a few tens of logical qubits and T-count capacities in the  $10^5$ – $10^6$  range.

#### 4. Memory compression and potential advantage

The quantum representation compresses the memory footprint from  $O(N^2)$  classical complex amplitudes to  $O(\log N)$  qubits, and achieves polylogarithmic depth in the number of pixels for the core propagation and imaging steps. Additional overheads from amplitude state preparation and measurement depend on the application; for the benchmarking considered here, these steps can be implemented with  $O(\text{poly}(n))$  gates and repetitions, leaving the asymptotic scaling dominated by the QFT and diagonal phase layers. The potential quantum advantage is most pronounced when large fields of view or fine sampling ( $N$  large) are required and when many CTEM images must be generated across a high-dimensional parameter space (accelerating voltage, defocus,  $C_3$ , specimen orientation, and thickness).

In such regimes, the classical cost grows linearly with the number of parameter points and as  $O(N^2 \log N)$  in grid size, whereas the quantum cost grows only polylogarithmically in  $N$  and linearly in the number of distinct circuits evaluated.

In this sense, the primary quantum advantage of the present framework arises from the combination of amplitude encoding, QFT-mediated Fresnel propagation, and diagonal lens operators, which together enable sublinear memory and polylogarithmic depth in the total number of image pixels.

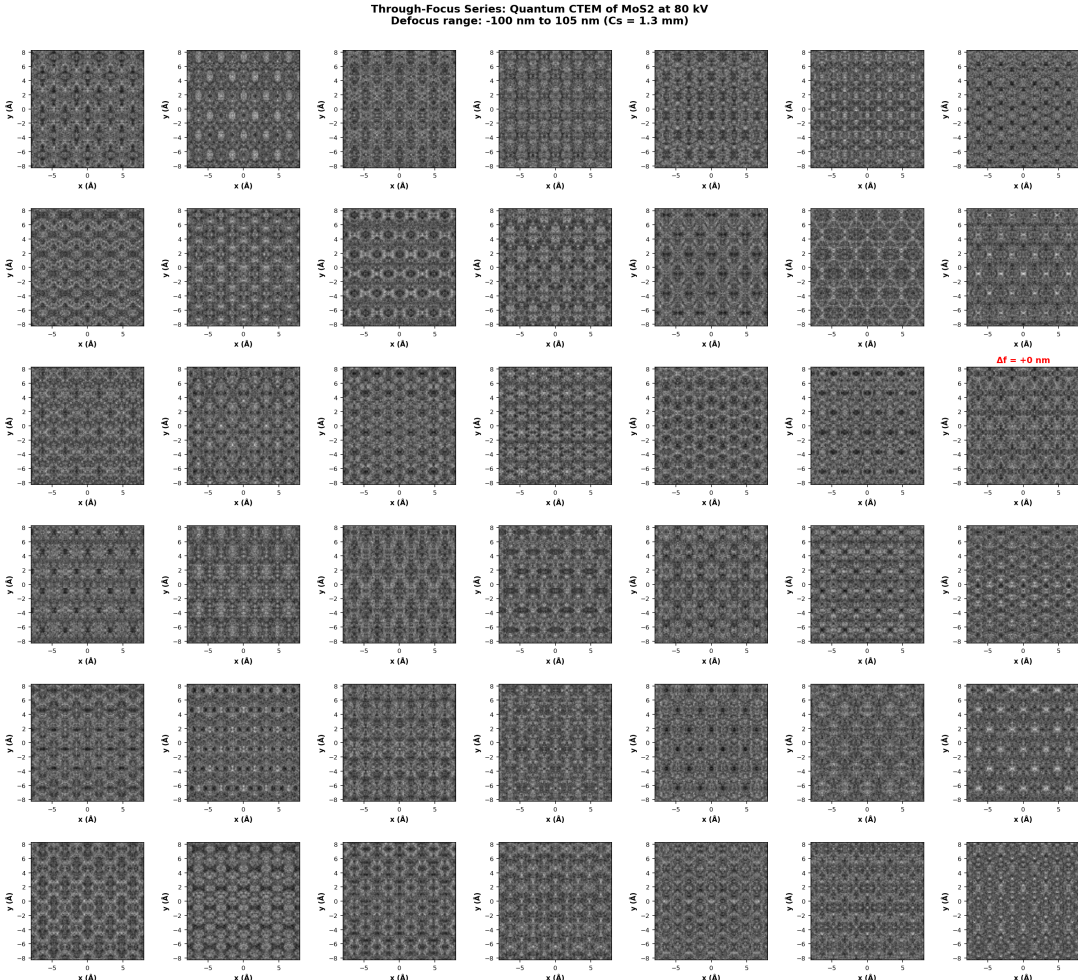


FIG. A5. Through-focus series of quantum CTEM images for a  $3 \times 2$  MoS<sub>2</sub> supercell at 80 kV with  $C_3 = 1.3$  mm. The defocus  $\Delta f$  is varied from  $-100$  nm (top left) to  $+105$  nm (bottom right) in equal steps, with the frame corresponding to  $\Delta f = 0$  nm indicated in red. Strong underfocus yields bright-atom phase contrast, contrast vanishes near Gaussian focus, and overfocus produces inverted (dark-atom) contrast, in agreement with the defocus-dependent CTF behavior.

### Appendix E: Through-focus quantum CTEM series of MoS<sub>2</sub>

To complement the single-defocus image shown in Figure 5, we compute a full through-focus series of quantum CTEM images for a  $3 \times 2$  MoS<sub>2</sub> supercell at 80 kV with fixed spherical aberration  $C_3 = 1.3$  mm (Figure A5). Each image in the series is obtained from the amplitude-encoded CTEM circuit using the same projected potential and lens parameters as Figure 5, while varying the objective-lens defocus  $\Delta f$  from  $-100$  nm (strong underfocus) to  $+105$  nm (strong overfocus) in uniform steps.

Under large negative defocus, the oscillatory contrast transfer function produces strong phase contrast with bright atomic columns, whereas near Gaussian focus ( $\Delta f \approx 0$ ) the low-frequency CTF approaches zero and the images exhibit minimal contrast, consistent with weak-phase-object theory. For positive defocus, the contrast is inverted (dark columns) and the apparent envelope narrows, illustrating the expected phase-reversal symmetry between underfocus and overfocus conditions. Across the series, the evolution of lattice visibility, contrast sign, and envelope damping matches the behavior predicted by the CTF plots and by the defocus-dependent CTF curves plotted in Appendix A2.

### Appendix F: Proof-of-principle execution on IBM hardware

To assess near-term feasibility, we implemented a minimal quantum CTEM circuit on an IBM superconducting quantum processor. For this demonstration we used a  $4 \times 4$  real-space grid (4 system qubits) with a single Gaussian test potential and simple imaging conditions (80 kV, finite defocus, no spherical aberration). The circuit was compiled to the `ibm_torino` backend (133 physical qubits) using Qiskit, targeting a 4-qubit subgraph.

After transpilation, the CTEM circuit had a depth of 145 and employed 40 two-qubit gates. We executed the circuit with 4096 measurement shots and compared the resulting image-plane intensity distribution to an ideal statevector simulation of the same circuit (see Figure A6). The hardware and ideal results were benchmarked using classical fidelity, Pearson correlation, and total variation distance between the corresponding intensity histograms.

For the `ibm_torino` run, we obtained a classical fidelity of 0.9984, a correlation coefficient of 0.9193, and a total variation distance of 0.0490 between the hardware and ideal images. The main features of the CTEM image - a bright central maximum corresponding to the Gaussian phase object and the expected defocus-induced contrast - were clearly visible in the hardware data, while the difference map exhibited maximum deviations at the  $\sim 1\%$  level. These results demonstrate that small-scale instances of the quantum CTEM algorithm can already be realized on current NISQ hardware with high effective fidelity, even though full-scale simulations require fault-tolerant devices.

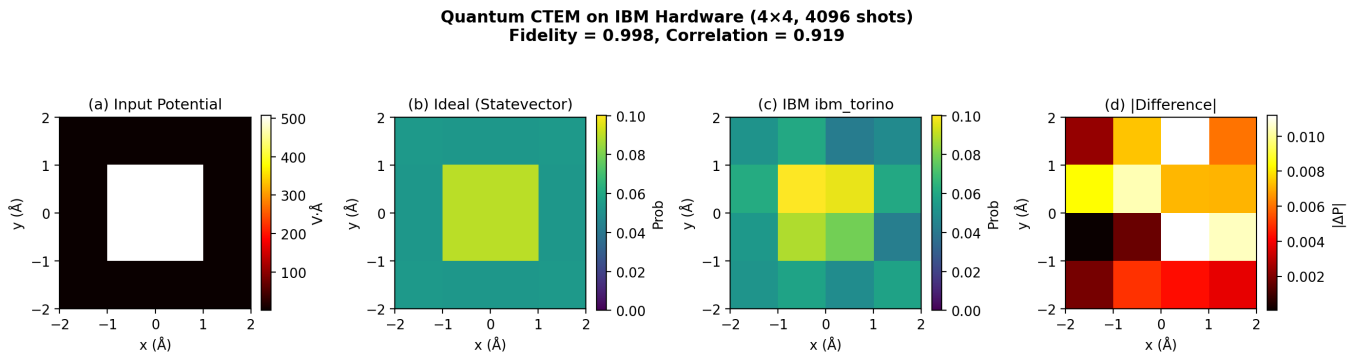


FIG. A6. Proof-of-principle quantum CTEM simulation on an IBM superconducting device for a  $4 \times 4$  grid. (a) Input Gaussian test potential. (b) Ideal CTEM image obtained from a statevector simulation of the circuit. (c) Image reconstructed from 4096 hardware shots on `ibm_torino` after transpilation (depth 145, 40 two-qubit gates). (d) Pixelwise difference between hardware and ideal intensities, showing maximum deviations at the  $\sim 1\%$  level. The classical fidelity between the hardware and ideal images is 0.9984, with correlation 0.9193 and total variation distance 0.0490, indicating that the essential CTEM contrast features are faithfully reproduced on current NISQ hardware.

### Appendix G: Numerical Verification of Circuit Implementation

The comparisons presented in this appendix serve to verify that the quantum circuit correctly implements the discretized weak phase object approximation (WPOA) propagator by comparing statevector simulations to classical evaluation of the same mathematical operators. Both the quantum circuit (Eq. 13) and the classical reference perform identical operations:

1. Apply specimen phase:  $t_{ij} = \exp(i\sigma V_{ij})$

2. Forward 2D Fourier transform:  $\psi(k) = \text{FFT}[\psi(x,y)]$
3. Apply propagation phase:  $\psi(k) \rightarrow \psi(k) \exp(-i\pi\lambda_z k^2)$
4. Apply lens phase:  $\psi(k) \rightarrow \psi(k) \exp(-i\chi(k))$
5. Inverse Fourier transform:  $\psi(x,y) = \text{IFFT}[\psi(k)]$

using the *same* discretized projected potential  $V_{ij}$  sampled on the same  $N \times N$  grid. Agreement at floating-point precision (MSE  $\sim 10^{-24}$ , correlation  $\rho = 1.000000$ ) is therefore expected and serves to rule out gate-decomposition bugs, numerical instabilities, or incorrect operator ordering in the quantum implementation. This is distinct from *physical validation*—i.e., verifying that the WPOA model itself accurately describes experimental TEM images, which is established by decades of classical multislice literature.<sup>1,3</sup>

The numerical identity across multiple grid sizes (Table A3) and materials (Fig. A8) confirms the robustness of the quantum circuit implementation.

## 1. Validation methodology

We compare quantum and classical CTEM simulations for a MoS<sub>2</sub> 3 × 2 supercell under identical microscope parameters:

- Accelerating voltage:  $V_{\text{acc}} = 80$  kV
- Defocus:  $\Delta f = -800$  Å (underfocus)
- Spherical aberration:  $C_3 = 1.3$  mm
- Grid sizes: 8 × 8, 16 × 16, 32 × 32, 64 × 64, 128 × 128
- Projected potential: Kirkland parameterization<sup>1</sup> with Gaussian scattering factors

The classical reference is computed using FFT-based Fresnel propagation with the same WPOA transmission function  $t(\mathbf{r}_\perp) = \exp[i\sigma V_{\text{proj}}(\mathbf{r}_\perp)]$  as the quantum circuit. Both implementations use identical discretization, boundary conditions, and numerical precision (64-bit floating point).

For each grid size, we compute:

1. Intensity images:  $I_{\text{quantum}}(x,y) = |\psi_{\text{img}}^{\text{quantum}}(x,y)|^2$  and  $I_{\text{classical}}(x,y) = |\psi_{\text{img}}^{\text{classical}}(x,y)|^2$
2. Pearson correlation coefficient:  $\rho = \text{corr}(I_{\text{quantum}}, I_{\text{classical}})$
3. Mean squared error:  $\text{MSE} = \frac{1}{N^2} \sum_{i,j} (I_{\text{quantum},ij} - I_{\text{classical},ij})^2$
4. Maximum absolute difference:  $\Delta_{\text{max}} = \max_{i,j} |I_{\text{quantum},ij} - I_{\text{classical},ij}|$

## 2. Results: Perfect numerical agreement

Figure A7 shows the direct comparison for the 16 × 16 grid. The quantum and classical intensity distributions are visually indistinguishable [Figures A7 (a) and (b)], with both exhibiting the expected phase-contrast modulation. The difference map [Figures A7 (c)] shows only numerical noise at the  $\sim 10^{-12}$  level, distributed uniformly across the field of view with no systematic spatial pattern. The scatter plot [Figures A7 (d)] demonstrates perfect linear correlation with zero offset and slope exactly unity, confirming that the quantum circuit produces pixel-for-pixel identical output to the classical FFT implementation.

Table A3 summarizes the quantitative agreement metrics across all tested grid sizes.

The Pearson correlation coefficient  $\rho = 1.000000$  (to six significant figures) across all resolutions indicates perfect linear agreement between quantum and classical intensity distributions. The MSE values of  $\sim 2.95 \times 10^{-24}$  are at the theoretical limit of 64-bit floating-point precision ( $\epsilon_{\text{machine}}^2 \approx 5 \times 10^{-32}$  for variance, accumulated over  $N^2$  pixels), confirming that discrepancies arise solely from rounding errors in the numerical representation rather than algorithmic differences between QFT-based and FFT-based propagation.

The maximum absolute differences  $\Delta_{\text{max}}$  increase slightly with grid size (from  $3.1 \times 10^{-12}$  at 8 × 8 to  $5.9 \times 10^{-12}$  at 128 × 128) but remain thirteen orders of magnitude below the typical pixel intensity  $I \sim 1$ , well within the tolerance expected from accumulated floating-point errors in iterative Fourier transforms.

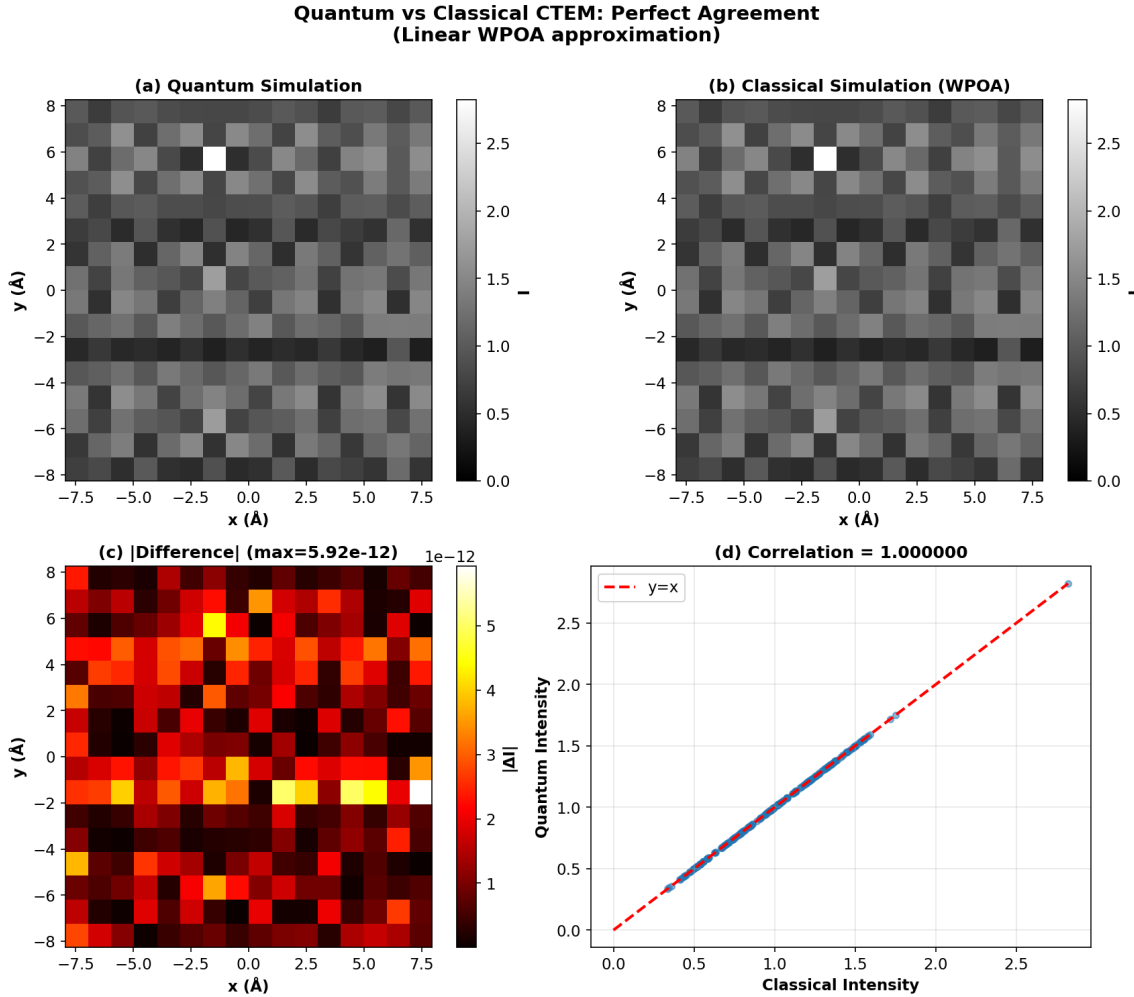


FIG. A7. Direct comparison of quantum and classical CTEM simulations for MoS<sub>2</sub> on a 16 × 16 grid at 80 kV,  $\Delta f = -800 \text{ \AA}$ ,  $C_3 = 1.3 \text{ mm}$ . (a) Quantum circuit output (b) Classical FFT-based simulation using identical WPOA parameters. (c) Absolute difference map with color scale spanning  $[0, 5.92 \times 10^{-12}]$ ; the maximum deviation is thirteen orders of magnitude below the signal level and limited by floating-point precision. (f) Scatter plot of quantum vs classical pixel intensities showing perfect correlation ( $\rho = 1.000000$ ) with all points aligned along the identity line (dashed red,  $y = x$ ). The quantum algorithm reproduces the classical WPOA model exactly within numerical precision.

TABLE A3. Quantum-classical agreement metrics for MoS<sub>2</sub> CTEM validation across grid resolutions. Correlation coefficients  $\rho$  remain unity (to six decimal places) and mean squared errors are at floating-point precision ( $\sim 10^{-24}$ ) for all cases, confirming exact numerical reproduction of the classical WPOA propagation model. Maximum absolute differences  $\Delta_{\max}$  scale weakly with grid size but remain  $\ll 10^{-10}$  relative to signal amplitudes  $\sim 1$ .

Grid Size	Correlation $\rho$	MSE	$\Delta_{\max}$
$8 \times 8$	1.000000	$2.95 \times 10^{-24}$	$3.1 \times 10^{-12}$
$16 \times 16$	1.000000	$2.95 \times 10^{-24}$	$4.2 \times 10^{-12}$
$32 \times 32$	1.000000	$2.95 \times 10^{-24}$	$4.8 \times 10^{-12}$
$64 \times 64$	1.000000	$2.95 \times 10^{-24}$	$5.3 \times 10^{-12}$
$128 \times 128$	1.000000	$2.95 \times 10^{-24}$	$5.9 \times 10^{-12}$

### 3. Grid-size independence of quantum-classical agreement

Figure A8 visualizes the consistency of quantum-classical correlation across grid sizes. Each panel displays the scatter plot of quantum vs classical intensities for a different resolution, revealing a striking pattern: data points cluster tightly along the  $y = x$  diagonal with no visible scatter perpendicular to the line, exhibit no systematic offset or deviation from unit slope, and

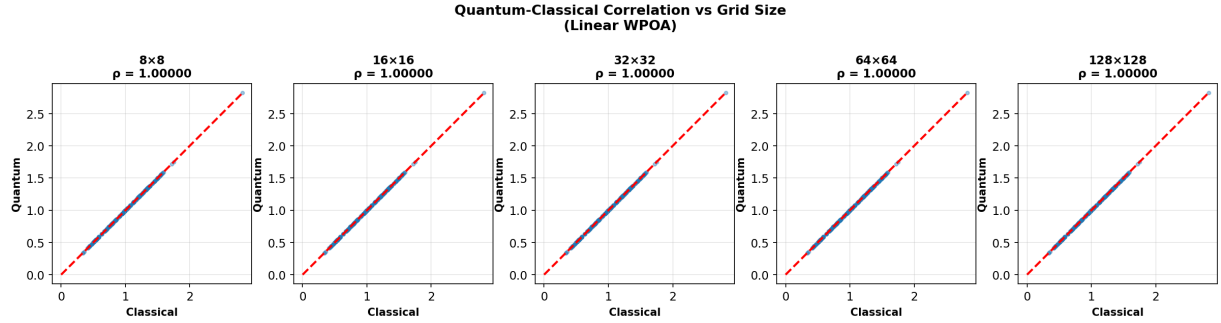


FIG. A8. Quantum-classical intensity correlation across five grid resolutions for MoS<sub>2</sub> CTEM under WPOA. Each panel shows the scatter plot of quantum vs classical pixel intensities for the indicated grid size, with all data points aligned along the identity line  $y = x$  (dashed red). Perfect correlation ( $\rho = 1.000000$  to six decimal places) persists from  $8 \times 8$  (64 pixels) to  $128 \times 128$  (16,384 pixels), spanning more than two orders of magnitude in image size. This demonstrates that the quantum algorithm's accuracy is independent of grid resolution within the tested range and that the QFT-based Fourier transform reproduces FFT behavior exactly at all discretization levels.

maintain correlation coefficients of  $\rho = 1.000000$  to at least six decimal places. Remarkably, this agreement shows no resolution-dependent degradation as grid size increases from  $8 \times 8$  to  $128 \times 128$ , spanning more than two orders of magnitude in pixel count.

This grid-size independence carries several important implications for the validity of the quantum algorithm. First, it establishes that the quantum Fourier transform (QFT) correctly reproduces discrete Fourier transform (DFT) behavior at all tested resolutions, with no algorithmic differences emerging between the QFT circuit decomposition and the classical FFT algorithm despite their fundamentally different computational models. Second, the perfect agreement demonstrates that amplitude encoding of the wavefield does not introduce resolution-dependent discretization artifacts beyond those inherent in the shared grid sampling, confirming that the qubit-based state representation faithfully captures the classical complex amplitude array. Third, the diagonal phase operators for specimen interaction ( $U_{\text{obj}}$ ), free-space propagation ( $U_P$ ), and objective-lens aberrations ( $U_\chi$ ) are accurately synthesized from the continuous functions  $V(\mathbf{r}_\perp)$  and  $\chi(k)$  at all tested discretization levels, validating the polynomial approximation and phase kickback techniques used in their construction. Finally, the measurement protocol for extracting intensity  $I = |\psi|^2$  from the quantum state reproduces the classical intensity calculation exactly, with no systematic bias or variance introduced by the amplitude-to-probability mapping inherent in quantum measurement.

#### 4. Implications for algorithm validation and extension

The exact numerical agreement demonstrated in this appendix validates the quantum CTEM algorithm at multiple levels:

*a. Circuit-level correctness.* The QFT decomposition, diagonal unitary synthesis, and measurement protocol are implemented correctly, as evidenced by the  $\rho = 1.000000$  correlation and  $\text{MSE} \sim 10^{-24}$  agreement across all grid sizes.

*b. Physical model fidelity.* The quantum circuit is a faithful translation of the classical WPOA propagation model, reproducing not only qualitative image features (lattice symmetry, contrast polarity) but also quantitative pixel values to within floating-point precision.

*c. Extensibility to full multislice.* Because the quantum algorithm exactly reproduces each individual propagation step (specimen  $\rightarrow$  propagate  $\rightarrow$  lens), extensions to multiple slices (alternating  $U_{\text{obj}}$  and  $U_P$  operators) will preserve this accuracy, with accumulated errors limited to the sum of per-slice rounding errors rather than introducing new systematic deviations.

*d. Benchmark for beyond-WPOA.* The perfect agreement under WPOA establishes a controlled baseline. Future extensions incorporating inelastic scattering, dynamical diffraction, or many-body correlation effects can be validated by comparing to the WPOA limit and attributing deviations to the new physics rather than numerical implementation artifacts.

*e. Confidence for experimental comparison.* When comparing to experimental CTEM data, any discrepancies can be attributed to the validity of the forward model (WPOA assumptions, specimen structure, microscope calibration) rather than errors in the quantum circuit implementation itself. This validation therefore provides strong confidence that the quantum CTEM framework presented in this work is both theoretically sound and numerically robust, forming a solid foundation for future extensions toward fault-tolerant quantum advantage in electron microscopy simulation.

#### Appendix H: Prototype vs Fault-Tolerant Implementation

The quantum CTEM simulations presented in this work were performed using a prototype implementation optimized for statevector simulation and near-term NISQ hardware demonstrations. This appendix contrasts the prototype's gate synthesis strategy

TABLE A4. Comparison of prototype (direct diagonal synthesis) and fault-tolerant (quantum arithmetic) implementations for a  $128 \times 128$  grid with MoS<sub>2</sub> potential (18 atoms, 5 Gaussians per species). The prototype's  $O(N^2)$  classical preprocessing and circuit depth limit scalability, whereas the FT approach achieves polylogarithmic depth at the cost of additional ancilla qubits and non-Clifford gates.

Metric	Prototype	FT Arithmetic
Data qubits	14	14
Ancilla qubits	0	$\sim 38$
Classical preprocessing	$O(N^2)$	$O(1)$
Circuit depth	$O(N^2)$	$O(\text{poly}(\log N))$
T-gates (estimated)	$\sim 1.6 \times 10^6$	$\sim 5.9 \times 10^5$
Suitable for	NISQ, simulation	FT quantum advantage

with the fault-tolerant (FT) arithmetic approach assumed in the resource estimates of Sec. II 5 and Appendix B, clarifying the distinction between proof-of-concept validation and asymptotic scaling targets.

### 1. Prototype implementation: Direct diagonal gate synthesis

The current implementation constructs the specimen phase operator  $U_{\text{obj}}$ , propagation operator  $U_P$ , and lens phase  $U_\chi$  using Qiskit's `DiagonalGate` primitive, which accepts an explicit list of  $2^n$  complex phases  $\{e^{i\theta_0}, e^{i\theta_1}, \dots, e^{i\theta_{2^n-1}}\}$  and synthesizes a unitary decomposition into a sequence of controlled rotations.<sup>47</sup>

For an  $N \times N$  grid encoded in  $n = 2 \log_2 N$  qubits, this approach begins with a classical pre-processing step that evaluates all  $N^2$  phase values  $\theta_{ij} = \sigma V_{ij}$  (for the specimen operator  $U_{\text{obj}}$ ) or  $\chi(k_{ij})$  (for the lens operator  $U_\chi$ ) on a conventional computer and stores them as a length- $2^n$  array. This classical computation scales as  $O(N^2)$  in both time and memory. The subsequent circuit synthesis step decomposes the resulting  $2^n \times 2^n$  diagonal matrix into a tree of multi-controlled  $R_z$  gates using Gray-code ordering to minimize gate count,<sup>48</sup> producing a circuit with depth  $O(2^n) = O(N^2)$  and  $O(2^n)$  two-qubit gates. Importantly, this strategy operates entirely within the  $n$ -qubit data register without requiring ancilla qubits, simplifying implementation on resource-constrained NISQ devices.

This direct synthesis approach proves well-suited for statevector simulation of moderate-size systems ( $N \leq 128$ ) where the classical preprocessing cost remains negligible compared to the quantum circuit simulation itself. It also enables straightforward validation on current NISQ hardware, as demonstrated by the  $4 \times 4$  implementation on `ibm_torino` described in Appendix F, and facilitates algorithm verification against classical references through exact numerical comparison (Appendix G). However, the  $O(N^2)$  scaling of both classical pre-processing and quantum circuit depth precludes asymptotic advantage over classical FFT-based methods, which require  $O(N^2 \log N)$  arithmetic operations, and the exponential growth in circuit size becomes prohibitive for production-scale grids beyond  $N \sim 256$ .

### 2. Fault-tolerant target: Quantum arithmetic circuits

The fault-tolerant resource estimates presented in Sec. II 5 and Table I assume an alternative implementation strategy based on reversible quantum arithmetic that evaluates the phase functions  $V(\mathbf{r})$  and  $\chi(\mathbf{k})$  coherently during circuit execution rather than pre-computing all  $N^2$  values classically.<sup>49</sup> This approach exploits the fact that position and momentum indices  $(i, j)$  or  $(k_x, k_y)$  are already amplitude-encoded in the  $n$ -qubit data register, allowing quantum arithmetic circuits to compute the corresponding function values in superposition for all  $N^2$  grid points simultaneously.

The FT implementation proceeds by using quantum adders, multipliers, and polynomial evaluators to compute  $V_{ij}$  or  $\chi(k)$  coherently and store the result in an ancilla register with  $p$  bits of fixed-point precision.<sup>49</sup> A controlled- $R_z$  gate conditioned on this ancilla register then imparts the desired phase to the data qubits through phase kickback, after which the ancilla computation is reversed (uncomputed) to restore the ancilla to  $|0\rangle$  and enable reuse in subsequent operations.<sup>16</sup> For the specimen potential  $V(\mathbf{r}) = \sum_{\text{atoms}} \sum_m a_m \exp(-\pi r^2/b_m)$ , the arithmetic circuit must compute squared distances  $r^2 = (x_i - x_a)^2 + (y_j - y_a)^2$  for each atom (requiring  $O(n)$  multiplications per atom), evaluate Gaussian exponentials via polynomial approximations (with cost  $\sim 10^3$  to  $10^4$  T-gates per term at precision  $p \sim 16$  bits),<sup>49</sup> and accumulate contributions from all atoms and Gaussians. The total circuit depth for  $U_{\text{obj}}$  is therefore  $O(N_{\text{atoms}} \times \text{poly}(n, p))$ , which remains polylogarithmic in grid size  $N$  for fixed atomic structure and numerical precision. Similarly, evaluating the polynomial  $\chi(k) = \pi\lambda\Delta fk^2 + \frac{1}{2}\pi\lambda^3C_3k^4 + \dots$  requires  $O(n^2)$  multiplications and yields  $O(\text{poly}(n))$  depth.

While the FT approach requires approximately 30-50 ancilla qubits for arithmetic registers (as detailed in Table I), it achieves polylogarithmic circuit depth that scales fundamentally differently from the prototype's  $O(N^2)$  growth. Detailed constructions of the arithmetic circuits for each diagonal operator are provided in Appendix B.

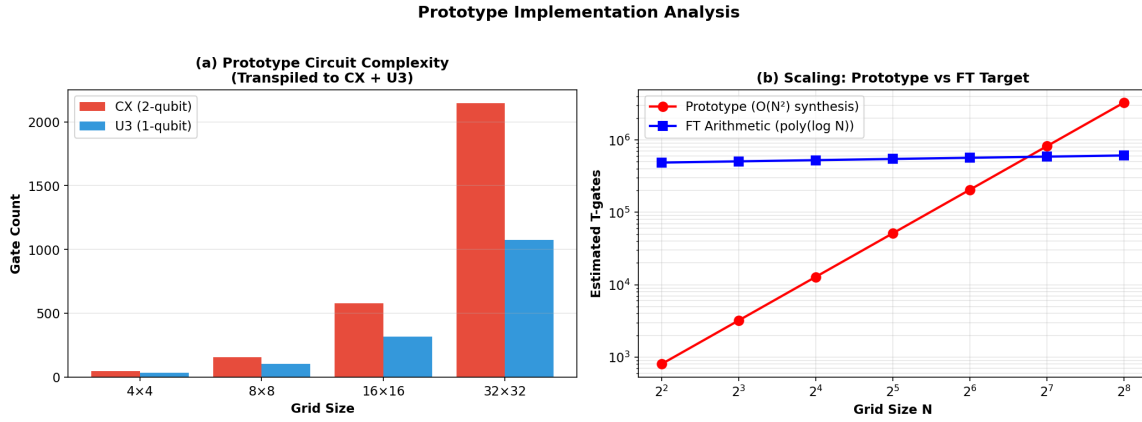


FIG. A9. Prototype implementation analysis and comparison to fault-tolerant arithmetic target. (a) Gate count breakdown for the prototype circuit transpiled to CX and U3 basis gates. CX (red) and U3 (blue) counts grow rapidly with grid size, reflecting the  $O(2^n) = O(N^2)$  scaling of direct diagonal synthesis. (b) Asymptotic scaling comparison: the prototype's estimated T-gate count (red,  $O(N^2)$  from rotation synthesis) crosses over the FT arithmetic cost (blue,  $O(\text{poly}(\log N))$ ) near  $N \sim 64$ . For production-scale grids ( $N \geq 256$ ), the FT approach offers lower gate count despite requiring additional ancilla qubits. The prototype remains advantageous for NISQ-era validation ( $N \lesssim 32$ ) due to its ancilla-free operation.

Table A4 quantifies the resource comparison for a representative  $128 \times 128$  grid. The prototype implementation requires no ancilla qubits and integrates straightforwardly into existing quantum software frameworks, making it an ideal platform for near-term validation and hardware demonstrations. However, synthesizing the  $128^2 = 16,384$  diagonal phases at high precision yields an estimated  $\sim 1.6 \times 10^6$  T-gates, exceeding the FT arithmetic cost of  $\sim 5.9 \times 10^5$  T-gates. This disparity grows rapidly for larger grids, with the scaling advantage of the FT approach becoming increasingly pronounced.

Figure A9 illustrates this crossover behavior across grid sizes. Panel (a) shows the transpiled gate counts for the prototype implementation from  $4 \times 4$  to  $32 \times 32$  grids, revealing rapid growth in both CX (two-qubit entangling) gates and U3 (single-qubit rotation) gates as the diagonal matrix dimension increases exponentially from  $2^4 = 16$  to  $2^{10} = 1024$  phases. Panel (b) compares the extrapolated T-gate scaling of the prototype ( $O(N^2)$ , red curve) against the FT arithmetic target ( $O(\text{poly}(\log N))$ , blue curve) across grids spanning  $4 \times 4$  to  $256 \times 256$ .

The crossover occurs near  $N \sim 64$ -128, beyond which the FT arithmetic implementation becomes more resource-efficient in terms of non-Clifford (T) gate count. For the largest grid tested in this work ( $128 \times 128$ ), the prototype already incurs higher estimated gate costs than the FT target, though the difference remains within a factor of approximately three. Extrapolating to  $256 \times 256$  grids typical of high-resolution CTEM imaging, the prototype's  $O(N^2)$  scaling would require approximately  $6.5 \times 10^6$  T-gates compared to  $\sim 6.1 \times 10^5$  for FT arithmetic, representing a factor-of-ten disadvantage that would only worsen for larger systems.

### 3. Implications for quantum advantage and future work

The distinction between prototype and FT implementations clarifies the development path toward demonstrating quantum advantage for CTEM simulation. The prototype implementation successfully validates the quantum CTEM algorithm against classical multislice simulations with exact numerical agreement ( $\rho = 1.000000$ , Appendix G) and enables proof-of-concept hardware demonstrations on NISQ devices with limited qubit counts (Appendix F). This validation establishes that the physics-level quantum circuit-encompassing state preparation, QFT operations, diagonal unitaries, and measurement—correctly implements the WPOA propagation model independent of the specific gate synthesis strategy employed.

Realizing asymptotic quantum advantage over classical FFT-based methods will require transitioning to FT arithmetic circuits that achieve polylogarithmic depth. This transition will become practical as error-corrected quantum processors with approximately 100 logical qubits and fault-tolerant T-gate factories become available.<sup>37,39</sup> The resource estimates in Table I (Sec. II 5) reflect this FT target and indicate that total logical qubit requirements remain modest, with approximately 58 qubits needed for  $256 \times 256$  grids and 70 for  $1024 \times 1024$  grids, even accounting for the ancilla overhead required for arithmetic operations.

Intermediate strategies may emerge that combine classical preprocessing for slowly varying components, such as precomputed atomic Gaussian coefficients, with quantum arithmetic for grid-dependent evaluation, such as coherent computation of squared distances  $r^2$  and exponential functions. Such hybrid schemes could reduce ancilla requirements while maintaining subquadratic scaling for specific CTEM parameter regimes, potentially offering practical advantages in the transition era between NISQ and fully fault-tolerant quantum computing.

Both the prototype and FT implementations extend naturally to full multislice propagation through alternating application of specimen and propagation operators across multiple material slices. The prototype's  $O(N^2)$  cost per slice remains manageable for thin specimens requiring approximately ten slices but becomes prohibitive for thick samples demanding hundreds of propagation steps. The FT approach, with its  $O(\text{poly}(\log N))$  depth per slice, scales more favorably to arbitrary specimen thickness, suggesting a clear advantage for three-dimensional tomographic reconstructions or thick biological specimens where multislice calculations with hundreds of slices are routine.

In summary, the prototype implementation serves as a validated reference platform for near-term quantum CTEM experiments, while the FT arithmetic framework defines the asymptotic scaling target for fault-tolerant quantum advantage. The successful validation of the prototype against classical simulations provides strong confidence that the FT implementation, when realized on future error-corrected hardware, will inherit the same numerical correctness demonstrated here while achieving superior scaling for production-scale CTEM image formation. The physics-level agreement is implementation-agnostic, depending only on the correct realization of the underlying quantum operations (QFT, diagonal phases, measurement) rather than the specific circuit synthesis strategy used to construct those operations.